Two-Way Blade Modeling Method for Structural Redesign of Compressor Blades

Solène Kojtych, Charles Audet, Alain Batailly

POLYTECHNIQUE MONTRÉAL
UNIVERSITÉ D'INGÉNIERIE

LABORATOIRE D'ANALYSE VIBRATOIRE ET ACOUSTIQUE

Two-way blade modelling method for the structural redesign of compressor blades

Solène Kojtych[1], Charles Audet[2], Alain Batailly[1]

Abstract

Over the past few years, stringent environmental requirements and the need for increased overall efficiency have forced designers to bring turbomachine components closer to their operating limits. To address lifespan issues, costly redesign operations are thus unavoidable. These operations face many roadblocks, especially when they are triggered by nonlinear phenomena for which there exists no design guidelines. For aircraft engine blades, the handling of nonlinear structural interactions is a major challenge. This works proposes a proof of concept for the redesign of compressor blades undergoing structural contact interactions at the blade-tip/casing interface. The redesign process involves the modelling of an existing input blade, followed by a shape update based on an iterative optimization algorithm. A two-way modelling method is proposed to parameterize the input blade and generate a CAD model from blade parameters describing several conical blade sections. The fidelity of the parameterized blade with respect to the input blade is assessed for the NASA blades rotor 37 and rotor 67. A high fidelity is observed with respect to geometric and dynamic characteristics. The modelling method is fully compatible with an iterative redesign process: it is applied to the redesign of rotor 37 to increase its robustness to contact interactions.

Keywords

compressor blade design, nonlinear structural interactions, parametric modeling, parameter extraction, shape optimization

1 - Department of Mechanical Engineering, École Polytechnique de Montréal, P.O. Box 6079, Succ. Centre-Ville, Montréal, Québec, Canada H3C 3A7
2 - GERAD and Mathematics and Industrial Engineering Department, Polytechnique Montréal, H3C 3A7, Montréal, Québec, Canada

Méthode de modélisation bidirectionnelle pour la reconception d'aubes de compresseurs

Solène Kojtych[1], Charles Audet[2], Alain Batailly[1]

Résumé

Ces dernières années, des exigences environnementales strictes et la nécessité d'accroitre les rendements ont poussé les concepteurs vers les limites de fonctionnement des composants de turbomachines. Pour prendre compte les problèmes liés à la durée de vie de ces composants, des opérations de reconception coûteuses sont inévitables. Celles-ci se heurtent à de nombreux obstacles, en particulier lorsqu'elles sont causées par des phénomènes non linéaires pour lesquels il n'existe pas de critères de conception. Pour les aubes de moteur d'avion en particulier, la gestion des interactions structurelles non linéaires est un défi majeur. Ce travail présente une preuve de concept pour la reconception d'aubes de compresseurs soumises à des interactions de contact entre le sommet d'aube et le carter. Le processus de reconception implique la modélisation d'une aube d'entrée existante, suivie d'une mise à jour de sa forme à l'aide d'un algorithme d'optimisation itératif. Une méthode de modélisation bidirectionnelle est proposée pour paramétrer une aube selon plusieurs sections coniques et générer un modèle CAO à partir des paramètres identifiés. La fidélité de l'aube paramétrée par rapport à l'aube d'entrée est évaluée pour les aubes NASA rotor 37 et rotor 67. Une grande fidélité des caractéristiques géométriques et dynamiques est observée. La méthode de modélisation est entièrement compatible avec un processus de reconception itératif : elle est appliquée à la reconception du rotor 37 afin d'accroître sa robustesse aux interactions de contact.

Mots-clés

conception d'aubes de compresseurs, interactions structurelles non linéaires, modélisation paramétrique, extraction de paramètres, optimisation de forme

1 - Département de génie mécanique, École Polytechnique de Montréal, P.O. Box 6079, Succ. Centre-Ville, Montréal, Québec, Canada H3C 3A7
2 - GERAD et département de mathématiques et génie industriel, École Polytechnique de Montréal, P.O. Box 6079, Succ. Centre-Ville, Montréal, Québec, Canada H3C 3A7

1 Introduction

Turbomachines are key components of both transportation and power generation industries. While safety concerns are essential in both these industrial domains, design processes of modern turbomachines are being transformed by recent and more constraining environmental regulations. As a matter of fact, in an increasingly competitive global market, reducing turbomachines environmental footprint has been driving research and development programs for many years [1]. The challenges faced by engineers and designers may vary depending on the industrial domain. In the power generation industry for instance, obvious material and economic constraints may prevent the replacement of existing facilities. For that reason, engineers' efforts are focused on expanding the lifespan of operating large gas turbines [2, 3]. In the aerospace industry however, the large production of new aircraft engines that must achieve lower emission levels, combined with critical mass constraints, call for the urgent evolution of specific design processes. In any case, engineers are facing a series of novel challenges that bring modern turbomachines closer to their operating limits: the lifespan of specific structural components may not be accurately assessed, which unavoidably yields costly redesign operations.

Broadly speaking, redesign operations may be triggered by different factors such as regulatory changes, the evolution of market demand [3], unsatisfactory performance [4] or lifespan issues [2]. In the worst-case scenario, redesign operations are needed following the failure of a given component with detrimental economic consequences as planes may be grounded or power plants stopped [2]. Beside their economic impact, redesign operations may be facing major roadblocks when their root cause is tied to sophisticated interactions that may arise within turbomachines and that are not yet fully understood. In particular, the mitigation of structural interactions—such as nonlinear vibrations of blades due to friction at the blade/disk interface [5] or structural contacts at the blade-tip/casing interface [6, 7] that must now be accounted for in non-accidental configurations—constitutes a major roadblock for designers. On the one hand, there exists no unified theoretical framework for the analysis of such nonlinear structural interactions. On the other hand, blade design procedures are essentially driven by aerodynamic considerations and are ill-suited to account for such phenomena. Designers thus rely on empirical (oftentimes linear) structural criteria and both design or redesign operations are time-consuming trial and error processes. A blade redesign process may be divided into three steps:

(1) modelling of the blade of interest, which is the focus of this work. Several reverse engineering methods may be used to model existing blades for redesign [8, 9], as well as for manufacturing [10], inspection [11] and maintenance [12] purposes. These methods aim at generating a Computed Aided Design (CAD) model from a point cloud obtained with experimental measurements of the blade. In most cases, the parameterization of this CAD model relies on purely geometrical parameters, such as control points of NURBS [13, 14, 15]. Some methods make it possible to extract engineering parameters with a more intuitive geometrical meaning, such as lean or sweep angles, in order to retrieve at best the original design intents. This may be done to compute a CAD model smoothed from measurements errors [16] or to analyze design trends on several blades [9]. However, only a few parameters, related to aerodynamic considerations, are deduced.

To the best of the authors' knowledge, a very limited number of published redesign studies relies on parameterization methods including both a procedure to extract engineering parameters with intuitive geometric meaning and a procedure to generate the corresponding CAD model [17, 18, 19]. In the work of Li *et al.* [18], a simplified design rule is introduced to map geometric and aerodynamic parameters to facilitate the update of the model with respect to aerodynamic considerations. Although aerodynamic performance is similar with the two parameterized models, the profile curves may be different. In another article, a parameterization was proposed for the optimization of blades accounting for contact interactions [20], but the geometry of the blade tip was simplified by the use of planar surfaces. Recently, high-fidelity parameterization methods have been proposed for aerodynamic studies [17, 19]. The need for methods linking several design steps has been underlined for the manufacturing of radial compressor impellers [19], which involves CAD, computational fluid dynamics and computer aided manufacturing models. As these methods are dedicated to specific applications, a case-by-case check of the influence of the chosen parameters on the phenomenon of interest is conducted, for instance to evaluate their impact on the flow control [17] or on the manufacturing quality [19].

(2) update of the blade. This step is often conducted empirically on the basis of previous studies and the expertise of designers [2, 3, 4, 21]. Alternately, design modifications may be carried out by iterative optimization

algorithms relying on successive performance simulations. Unconventional solutions of the space of parameters may thus be explored, in particular when the physical phenomena involved in the redesign are not fully understood. In the context of aerodynamic studies, evolutionary algorithms [13] are widely used, as well as adjoint approaches requiring the shape derivatives with respect to geometric parameters [22]. More recently, structural optimizations were conducted with blackbox optimization methods dedicated to time-consuming simulations for which the derivatives of the quantities of interest are not available [20].

(3) performance check of the updated blade, relying on numerical simulations [4, 21] or experimental tests at operating conditions [2, 3]. The performance check is often used to analyze features which were not explicitly accounted for in the redesign process [3, 21, 23]. This step may be required to assess the relevance of design modifications when an empirical update has been conducted [2, 4]. It may also be required following an iterative update when simplified simulations or empirical quantities, also called surrogates, are used to accelerate the optimization process [13, 20].

In this paper, the focus is made on the redesign operation of compressor blades undergoing structural contact interactions at the blade-tip/casing interface. Nonlinear vibrations subsequent to such interactions have been investigated for many years in both aircraft engines and large gas turbines. Indeed, these interactions are unavoidably favored by tighter operating clearances that must be achieved for increasing the turbomachine overall energy efficiency [24]. Recent advances in terms of numerical modelling led to the development of predictive numerical methodologies [25, 26, 27, 28] that were successfully confronted to experimental observations [28, 29, 30] or cross validated with other methods [31]. As of today, these methodologies have never been integrated within blades' design procedures. To the knowledge of the authors, they have only been employed for an *a posteriori* discrimination of selected blade profiles [20, 21]. In order to fully benefit from these numerical developments at the design stage, specific criteria—*i.e.* quantities characterizing the contact robustness—must be defined. However, confidentiality requirements associated to redesign procedures and contradictory aerodynamic and structural design recommendations [32] stymie a straightforward integration of such criteria in the design process. As a first step, new design tools are required to better understand links between design parameters of aircraft engine blades and their vibration response to contact interactions.

The objective of this work is to propose a proof of concept for the redesign of blades in order to enhance their robustness to contact interactions. An update step relying on an optimization process is considered, which requires a method to parameterize an existing blade and to iteratively generate blade models. Considering the confidentiality requirements on proprietary parameterized models, the existing blade is assumed to be a CAD model in this work. Consequently, this work focuses on the development of a two-way modelling method which aims at (1) extracting intuitive blade parameters from an input CAD model and (2) generating a parameterized CAD model and its Finite Element (FE) mesh in an iterative update context.

The proposed two-way modelling method represents the original contribution of the present work and aims at filling the gap between predictive methodologies and design aspects in the context of contact interactions. Overall, and contrary to previous published works [20, 33], the presented method is readily applicable to industrial blade models.

As the proposed methodology relies on a parameterization which is the corner stone of the redesign process, it must meet several criteria related to:

fidelity: the existing blade, called the input blade, and the computed parameterized blade should exhibit similar mechanical behavior, which requires similarity between geometries but also between dynamic properties.

resolution: a minor change in the parameters should be reflected in the CAD model, and vice versa to ensure the accuracy of the modelling step.

robustness: the parameterized CAD model and the FE mesh should be generated without errors from a wide range of blade parameters.

interpretability: the parameters should have an intuitive geometric and engineering meaning to ease the understanding of geometric trends on optimized blades at the performance check step.

versatility: the parameterization should comply with the standards of the domain, such as smoothness requirements of blade surface, and with the optimization method considered at the update step.

computational efficiency: the execution time for the parameters extraction and model generation should be low

with respect to the computation time of the update step.

The remainder of this work is organized as follows. In Sec. 2, the proposed two-way modelling method is described. An in-depth validation of the method is conducted in Sec. 3 from the parameterized models of NASA rotor 37 [34] and NASA rotor 67 [35]. The applicability on the tool in a redesign process is demonstrated in Sec. 4 and conclusions and future works are given in Sec. 5.

2 Two-way modelling method

The proposed two-way modelling method is implemented as a numerical tool featuring three modules:
`PAR` : a parameterization module to extract blade parameters from a CAD model,
`GEN` : a generation module to compute a CAD model from blade parameters,
`MSH` : a mesh module to generate a FE mesh from a CAD model.

The tool is entirely automated, it is implemented using the Python 3 language. CAD models and FE meshes are computed with the open-source software package Salome 9.7[1] to ensure the portability and integration of the tool in both academical and industrial computing environments. Particular attention is paid to its robustness and computational efficiency.

The redesign process considered in this work is summarized in Fig. 1, where the developed modules appear as colored boxes. The modelling step refers to the parameterization of a CAD model, which may be obtained by reverse engineering methods mentioned in Sec. 1. With respect to the update step, the blackbox optimization algorithm Mads [36], that has already been successfully employed for the optimization of blades with respect to contact interactions [20], is used. The redesign process relies on a blade parameterization partially inspired from previous work [20].

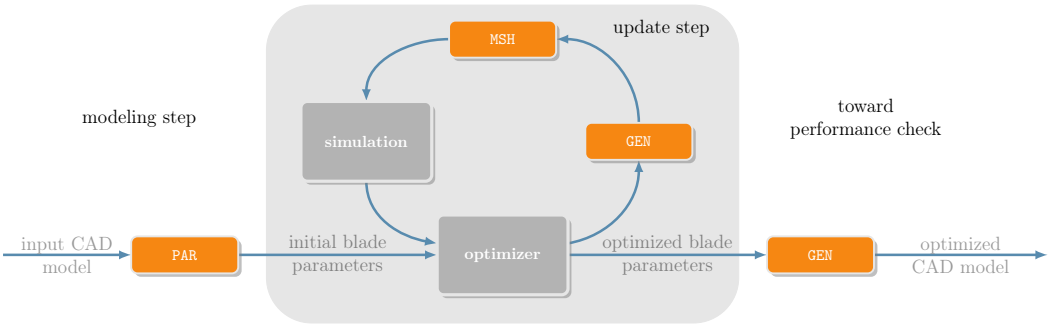

Figure 1. Description of the proposed redesign methodology.

In the current work, the parameterization describes the intersections of a blade with conical surfaces, called conical sections. When the conical surface is actually a cylindrical surface, the term cylindrical section is used. A blade is described by n_{sec} sections distributed along its height; three sections are depicted in Fig. 2. Each section is defined by stacking and profile parameters. The stacking parameters control the position of the section and the definition of the related conical surface. The profile parameters control the shape of the unwrapped section, called profile.

The blade parameters are defined in Sec. 2.1 and the FE mesh and CAD generation are described in Sec. 2.2. The extraction procedure is described in Sec. 2.3.

2.1 Blade parameterization

Blade sections are numbered using the index $i \in \{1, ..., n_{\text{sec}}\}$ from the hub to the top of the blade. Blade parameters are defined in different bases introduced in Sec. 2.1.1: the stacking parameters are defined in Sec. 2.1.2 and the profile parameters in Sec. 2.1.3.

[1] `https://www.salome-platform.org/`

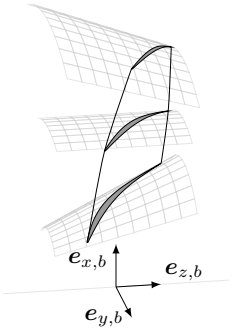

Figure 2. Blade with three sections: at the hub, mid-span and top of the blade.

2.1.1 Bases and notations

Rigorous mathematical notations are required to define the geometric quantities used in this work. Let $\boldsymbol{q}^i$ denote a reference point of section i, such as the centre of mass of the section in a given basis. A three-dimensional Cartesian basis is denoted $\mathcal{B}_\bullet = (\boldsymbol{o}_\bullet, \boldsymbol{e}_{x,\bullet}, \boldsymbol{e}_{y,\bullet}, \boldsymbol{e}_{z,\bullet})$, where $\boldsymbol{e}$ is a unit vector. A point $\boldsymbol{m}$ in this basis is defined by the coordinates $\boldsymbol{m}|_{\mathcal{B}_\bullet} = (m_{x,\bullet}, m_{y,\bullet}, m_{z,\bullet})$. The cylindrical basis with same origin and same longitudinal axis $\boldsymbol{e}_{z,\bullet}$ is denoted by $\mathcal{B}'_\bullet = (\boldsymbol{o}_\bullet, \boldsymbol{e}_{r,\bullet}, \boldsymbol{e}_{\theta,\bullet}, \boldsymbol{e}_{z,\bullet})$. A point $\boldsymbol{m}$ in $\mathcal{B}'_\bullet$ is written $\boldsymbol{m}|_{\mathcal{B}'_\bullet} = (m_{r,\bullet}, m_{\theta,\bullet}, m_{z,\bullet})$; the angle $m_{\theta,\bullet}$ is defined from axis $\boldsymbol{e}_{x,\bullet}$ in the plane $(\boldsymbol{o}_\bullet, \boldsymbol{e}_{x,\bullet}, \boldsymbol{e}_{y,\bullet})$ in the forward direction. The three-dimensional bases used in this work are presented in Fig. 3 for $n_{\text{sec}} = 3$ and described hereafter:

blade basis $\mathcal{B}_b(\boldsymbol{q})$, abbreviated $\mathcal{B}_b$, defined with respect to an arbitrary blade point $\boldsymbol{q}$ so that the blade turns in the forward direction around the $(\boldsymbol{o}_b, \boldsymbol{e}_{z,b})$ axis, $\boldsymbol{q}$ belongs to the $(\boldsymbol{o}_b, \boldsymbol{e}_{x,b})$ axis and the flow circulates along $\boldsymbol{e}_{z,b}$.

wrapped surface bases $\mathcal{B}_{s^i}$ of sections $i \in \{1, ..., n_{\text{sec}}\}$ such that $\boldsymbol{o}_{s^i}$ belongs to the rotation axis, $\boldsymbol{e}_{z,s^i} = \pm\boldsymbol{e}_{z,b}$ and $\boldsymbol{e}_{x,s^i} = \boldsymbol{e}_{x,b}$. For a conical section, $\boldsymbol{o}_{s^i}$ is the origin of the cone and $\boldsymbol{e}_{z,s^i}$ is oriented in the opening direction: the section is positive if $\boldsymbol{e}_{z,s^i} = \boldsymbol{e}_{z,b}$ and negative if $\boldsymbol{e}_{z,s^i} = -\boldsymbol{e}_{z,b}$. For a cylindrical section, $\boldsymbol{e}_{z,s^i} = \boldsymbol{e}_{z,b}$ and considering an arbitrary point $\boldsymbol{k}^i$ of the wrapped surface, $\boldsymbol{o}_{s^i}$ is chosen such that $k^i_{x,s^i} = 0$. In Fig. 3, $\boldsymbol{k}^2 = \boldsymbol{q}^2$.

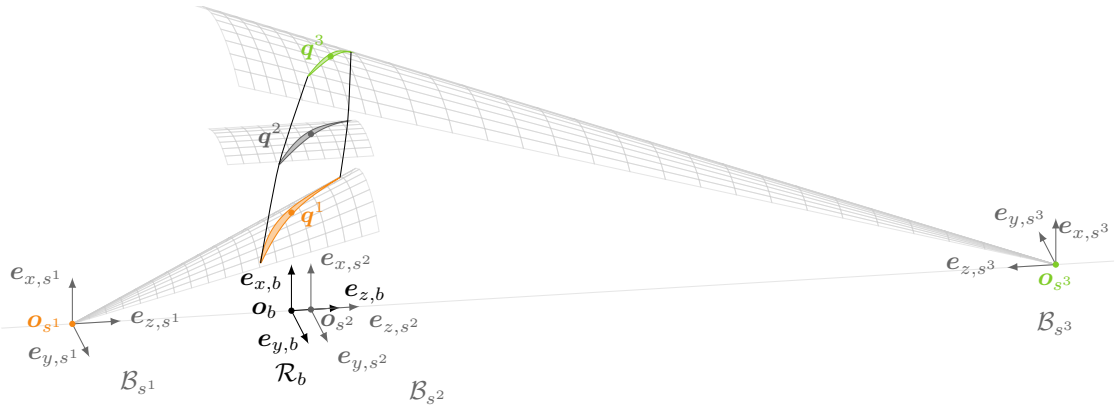

Figure 3. Blade basis $\mathcal{B}_b$ and wrapped surface bases $\mathcal{B}_{s^1}, \mathcal{B}_{s^3}$ of conical sections and $\mathcal{B}_{s^2}$ of a cylindrical section.

A two-dimensional Cartesian basis is denoted $\mathcal{P}_\bullet = (\boldsymbol{o}_\bullet, \boldsymbol{e}_{u,\bullet}, \boldsymbol{e}_{v,\bullet})$ and the associated polar coordinate system $\mathcal{P}'_\bullet = (\boldsymbol{o}_\bullet, \boldsymbol{e}_{r,\bullet}, \boldsymbol{e}_{\theta,\bullet})$, such that the angle $m_{\theta,\bullet}$ is defined from $\boldsymbol{e}_{u,\bullet}$ in the counterclockwise direction. The two-dimensional bases are:

unwrapped surface bases $\mathcal{P}_{d^i}$ of sections $i \in \{1, ..., n_{\text{sec}}\}$, see Fig. 4. A conical section is unwrapped such that the image of the point $\boldsymbol{o}_{s^i}$ is the point $\boldsymbol{o}_{d^i}$ and the image of a section point $\boldsymbol{m}|_{\mathcal{B}_{s^i}}$ satisfying $m_{y,s^i} = 0$ is a point on the $(\boldsymbol{o}_{d^i}, \boldsymbol{e}_{u,d^i})$ axis. For a cylindrical section, the image of the point $\boldsymbol{p}|_{\mathcal{B}'_{s^i}} = (r^i, 0, 0)$ is $\boldsymbol{o}_{d^i}$, where r^i

is the cylinder radius, and the image of $\boldsymbol{m}|_{\mathcal{B}_{s^i}}$ is a point on the $(\boldsymbol{o}_{d^i}, \boldsymbol{e}_{u,d^i})$ axis.

profiles basis $\mathcal{P}_p$ depicted in Fig. 5. For each profile i, the point $\boldsymbol{a}^i|_{\mathcal{P}_p}$ at the leading edge is at the origin and the point $\boldsymbol{b}^i|_{\mathcal{P}_p}$ at the trailing edge belongs to the $(\boldsymbol{o}_p, \boldsymbol{e}_{u,p})$ axis. These points are defined in Sec. 2.1.3.

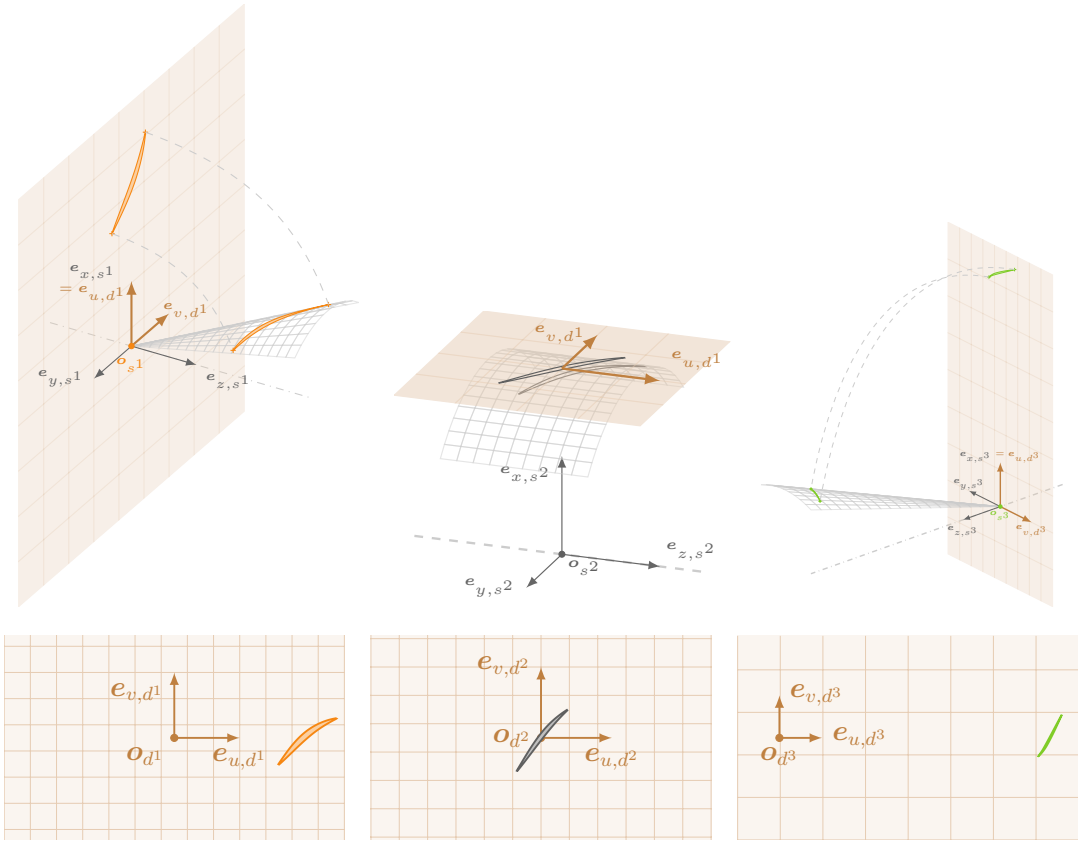

(a) positive conical section **(b)** cylindrical section **(c)** negative conical section

Figure 4. Wrapped surface bases $\mathcal{B}_{s^i}$ and unwrapped surface bases $\mathcal{P}_{d^i}$, $i \in \{1, 2, 3\}$.

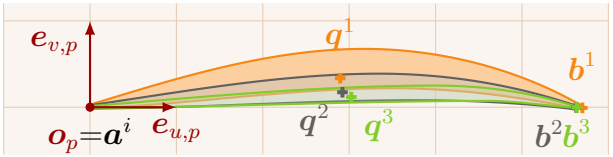

Figure 5. Profiles basis $\mathcal{P}_p$.

2.1.2 Stacking parameters

Five stacking parameters define the position and orientation of each section $i \in \{1, ..., n_{\text{sec}}\}$ in $\mathcal{B}_b$, see Fig. 6 and Table 1. The radius r^i, the lean angle $\Delta\theta^i$ and the sweep distance Δz^i define the position of the point $\boldsymbol{q}^i$:

$$r^i = q^i_{r,b}, \tag{1}$$

$$\Delta\theta^i = q^i_{\theta,b} - q^1_{\theta,b}, \tag{2}$$

Table 1. Section parameters.

type	name	symbol
stacking	radius	r^i
	sweep distance	Δz^i
	lean angle	$\Delta\theta^i$
	conicity	γ^i
	stagger angle	λ^i
profile	suction point abscissa	$s^i_{u,p}$
	suction point ordinate	$s^i_{v,p}$
	pressure point abscissa	$p^i_{v,p}$
	chord	c^i
	thickness between suction point and pressure point	t^i
	major radius upper ellipse	$r^i_{LE^+}$
	major radius lower ellipse	$r^i_{LE^-}$
	circle radius	r^i_{TE}
	blade inlet angle	ϕ^i_{LE}
	inlet upper wedge angle	$\psi^i_{LE^+}$
	inlet lower wedge angle	$\psi^i_{LE^-}$
	blade outlet angle	ϕ^i_{TE}
	outlet upper wedge angle	$\psi^i_{TE^+}$
	outlet lower wedge angle	$\psi^i_{TE^-}$

$$\Delta z^i = q^i_{z,b} - q^1_{z,b}. \tag{3}$$

The lean angle is positive in the direction of rotation of the blade. By definition of $\mathcal{B}_b(\boldsymbol{q})$, the radius r^i is not affected by the choice of $\boldsymbol{q}$ and the quantities $\Delta\theta^i$ and Δz^i are relative to the hub section. These three parameters are then independent from the chosen point $\boldsymbol{q}$.

The wrapped surface supporting a section is generated by the rotation around the $\boldsymbol{e}_{z,b}$ axis of a generatrix contained in the half-plane $\{\boldsymbol{m} \in \mathbb{R}^3 : m_{y,b} = 0, m_{x,b} > 0\}$ depicted in Fig. 7. The angle between the $\boldsymbol{e}_{z,b}$ axis and the generatrix is controlled by the conicity parameter $\gamma^i \in]-\frac{\pi}{2}, \frac{\pi}{2}[$:

$$\gamma^i = \widehat{\boldsymbol{e}_{z,b}, \boldsymbol{v}},$$

where $\boldsymbol{v}$ is a vector of the generatrix such that $v_{x,b} > 0$. When γ^i is null, the wrapped surface is a cylinder[2], otherwise, it is a cone. By definition, the angle γ^i is independent of the point $\boldsymbol{q}$ defining the basis $\mathcal{B}_b(\boldsymbol{q})$.

Finally, the orientation of the section on the wrapped surface is controlled by the stagger angle λ^i, defined in the basis $\mathcal{P}_{d^i}$ from the angle of the chord. The chord is given by the unit vector:

$$\boldsymbol{w}^i = \frac{\boldsymbol{b}^i|_{\mathcal{P}_{d^i}} - \boldsymbol{a}^i|_{\mathcal{P}_{d^i}}}{\|\boldsymbol{b}^i|_{\mathcal{P}_{d^i}} - \boldsymbol{a}^i|_{\mathcal{P}_{d^i}}\|}. \tag{4}$$

[2]In the implementation, a section is defined as cylindrical if $\gamma^i \leq 10^{-3}$ rad to prevent numerical errors associated to changes of basis from $\mathcal{B}_{s^i}$ to $\mathcal{P}_{d^i}$, see 5.1.2.

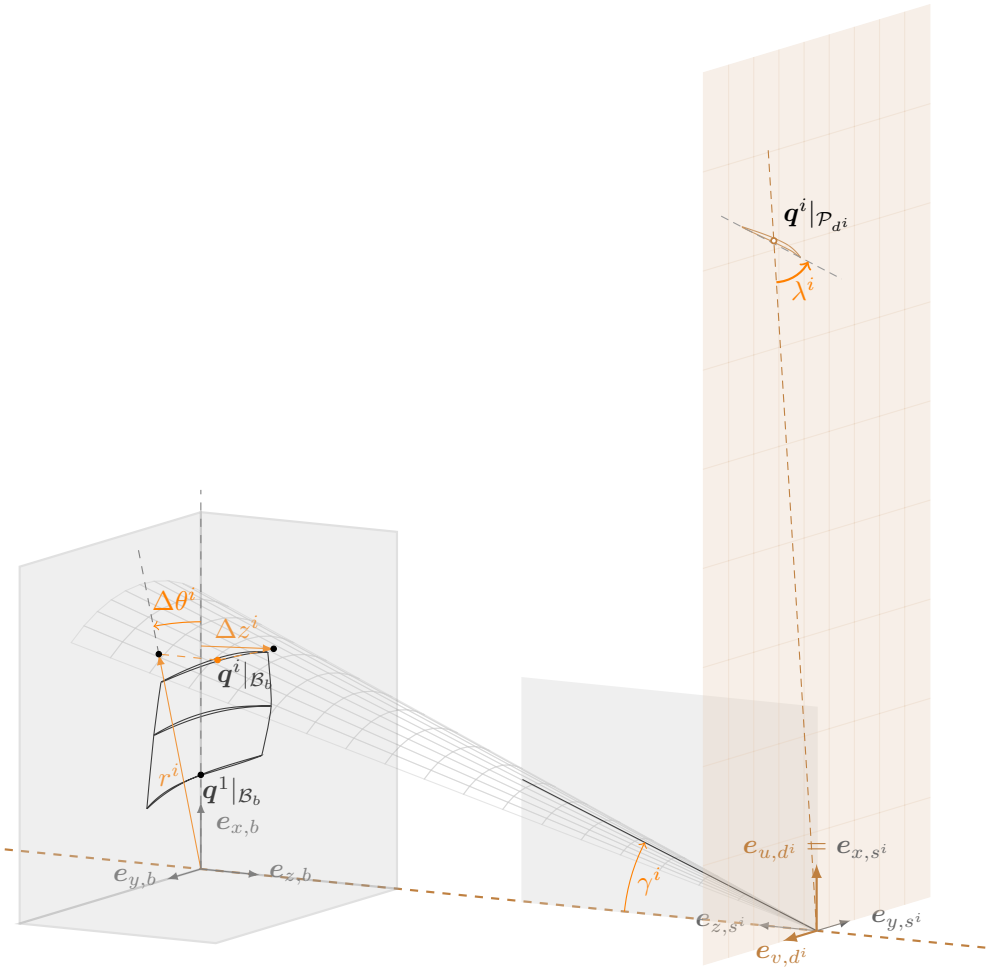

Figure 6. Representation of the stacking parameters.

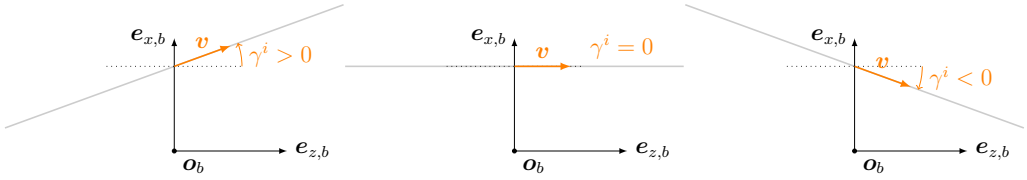

(a) positive conical section **(b)** cylindrical section **(c)** negative conical section

Figure 7. Conicity parameter γ^i and wrapped surface generatrix (——) with respect to the section type.

The setting angle $\lambda^i \in]0, \frac{\pi}{2}[$ depicted in Fig. 8 is then defined by:

$$\lambda^i = \begin{cases} (\widehat{\boldsymbol{v}^i, \boldsymbol{w}^i}) & \text{for a positive conical section,} \\ (\widehat{-\boldsymbol{v}^i, \boldsymbol{w}^i}) & \text{for a negative conical section,} \\ (\widehat{\boldsymbol{e}_{u,d^i}, \boldsymbol{w}^i}) & \text{for a cylindrical section,} \end{cases} \tag{5}$$

where $\boldsymbol{v}^i = \boldsymbol{q}^i|_{\mathcal{P}_{d^i}} / \|\boldsymbol{q}^i|_{\mathcal{P}_{d^i}}\|$ is a unit direction vector of the generatrix for conical sections. By definition, the angle

λ^i is independent from the point $\boldsymbol{q}$.

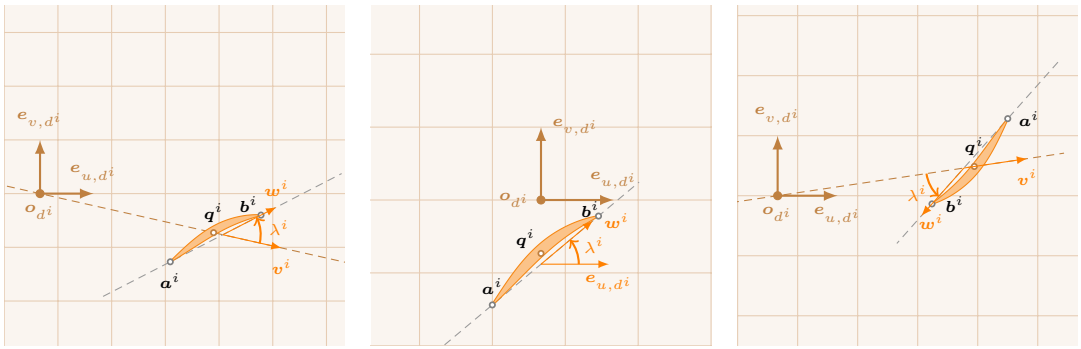

(a) positive conical section ($\gamma^i > 0$) **(b)** cylindrical section ($\gamma^i = 0$) **(c)** negative conical section ($\gamma^i < 0$)

Figure 8. Stagger angle λ^i with respect to the section type (the magnitude of unit vectors is exaggerated).

2.1.3 Profile parameters

The profile of section $i \in \{1, ..., n_{\text{sec}}\}$ is drawn with 7 curves depicted in Fig. 9 and described in a previous publication [20]. At the leading edge, two distinct elliptical arcs (1), (2) are used to model independent curves on the pressure and suction sides. The trailing edge, assumed to be small, is modeled by a unique circular arc (3). Suction and pressure sides are represented by two cubic splines each ((4), (5), (6), (7)). The suction point $\boldsymbol{s}^i$ and pressure point $\boldsymbol{p}^i$ are defined as the linking points of the splines, the linking point of ellipses is called $\boldsymbol{a}^i$ and $\boldsymbol{b}^i$ is the trailing edge point the furthest from $\boldsymbol{a}^i$.

To reduce the range of admissible parameters, assumptions on the curves are made. The profile is a $\mathcal{G}^1$ curve[3], horizontal tangents are imposed at points $\boldsymbol{s}^i$ and $\boldsymbol{p}^i$, the ellipsis axis ratio is fixed to 2 and $\boldsymbol{a}^i$ is fixed at the origin of $\mathcal{P}_p$. In order to improve further the parameterization, it is imposed in this work that the center of the trailing edge circle belongs to the abscissa axis. Thus, the orientation of the profile on the wrapped surface is decoupled from profile parameters and is only defined by the stagger angle λ^i.

In total, 14 parameters depicted in Fig. 9 are thus required to model a profile. The angles are considered positive such as represented and all parameters are defined in Table 1. All profile parameters are independent from the point $\boldsymbol{q}$ defining the blade basis $\mathcal{B}_b(\boldsymbol{q})$.

2.2 Parameterized model generation (`GEN` and `MSH` modules)

The aim of the `GEN` and `MSH` modules is to generate a CAD model and the corresponding FE mesh from the blade parameters, *i.e.* the n_{sec} sets of section parameters defined in Table 1. Sec. 2.2.1 describes the generation and discretization of the profiles based on profile parameters. Sec. 2.2.2 describes the positioning of the resulting point clouds according to the stacking parameters. Finally, Sec. 2.2.3 and 2.2.4 describe the generation of CAD model and FE mesh. For illustration purpose, these steps are conducted from the blade parameters given in 5.2 describing three sections at hub, mid-span and top of the blade rotor 37. These parameters were obtained by application of the extraction procedure described in Sec. 2.3.

2.2.1 Profile generation

The profile of each section $i \in \{1, ..., n_{\text{sec}}\}$ is drawn in $\mathcal{P}_p$ from profile parameters and discretized with the sampling length $c^i/1200$. This value was found to be small enough to ensure a fine representation of the profiles. This results in n_{sec} point clouds, from which the coordinates $\boldsymbol{q^i}|_{\mathcal{P}_p}$ of reference points in $\mathcal{P}_p$ are computed. The point $\boldsymbol{q^i}|_{\mathcal{P}_p}$ is chosen as the barycenter of the point cloud of section i in $\mathcal{P}_p$. For the considered example, the point clouds contain approximately 2500 points each and the profiles are depicted in Fig. 5.

[3] A curve is of regularity class $\mathcal{G}^n$ it the n-nth derivatives vectors are equal in direction, but not necessarily in norm.

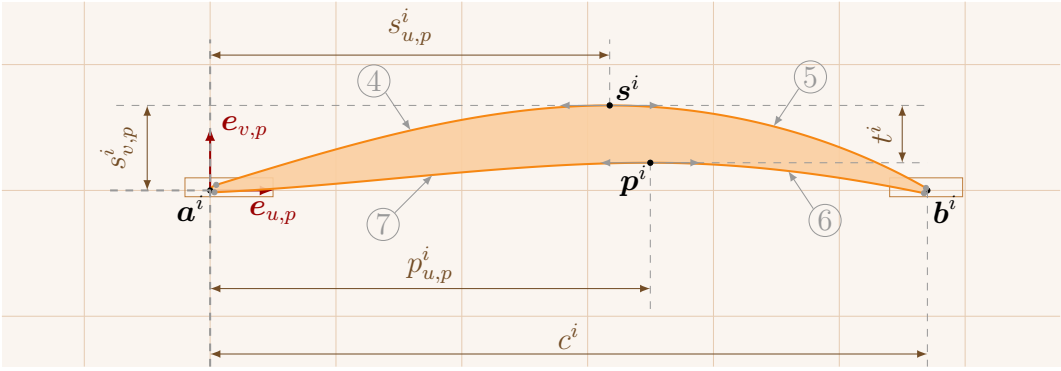

(a) blade profile

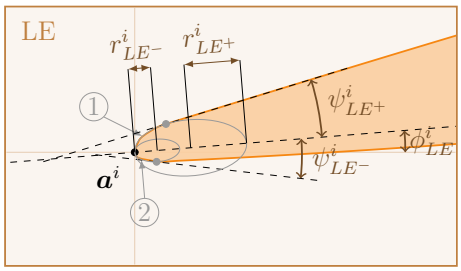

(b) zoom on the leading edge

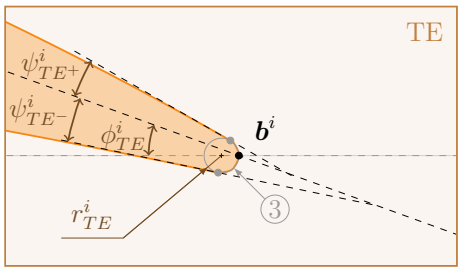

(c) zoom on the trailing edge

Figure 9. Representation of profile parameters.

2.2.2 Stacking of the sections

The point clouds of all sections are projected from the basis $\mathcal{P}_p$ to the blade basis $\mathcal{B}_b(\boldsymbol{q}^1)$ by three changes of basis summarized in Fig. 10. The change of basis equations are detailed in 5.1 and require equation parameters that must be computed from the stacking parameters of each section.

At step (1) in Fig. 10, the coordinates of an arbitrary section point $\boldsymbol{n}^i$ in $\mathcal{P}_p$ and $\mathcal{P}_{d^i}$ are required as well as the orientation of the chord or the profile in $\mathcal{P}_{d^i}$, given by the vector $\boldsymbol{w}^i|_{\mathcal{P}_{d^i}}$. The point $\boldsymbol{n}^i$ is chosen such that $\boldsymbol{n}^i = \boldsymbol{q}^i$, thus the coordinates $\boldsymbol{q}^i|_{\mathcal{P}_p}$ are known and the coordinates $\boldsymbol{q}^i|_{\mathcal{P}_{d^i}}$ are computed from the stacking parameters. For a conical section, the equation parameters are computed by:

$$q^i_{u,d^i} = \frac{r^i}{\sin|\gamma^i|}\cos(-\operatorname{sgn}(\gamma^i)\Delta\theta^i\sin|\gamma^i|), \tag{6}$$

$$q^i_{v,d^i} = \frac{r^i}{\sin|\gamma^i|}\sin(-\operatorname{sgn}(\gamma^i)\Delta\theta^i\sin|\gamma^i|), \tag{7}$$

$$(\widehat{\boldsymbol{e}_{u,d^i}, \boldsymbol{w}^i}) = \begin{cases} -\operatorname{sgn}(\gamma^i)\Delta\theta^i\sin|\gamma^i| + \lambda^i & \text{for positive conical section,} \\ -\operatorname{sgn}(\gamma^i)\Delta\theta^i\sin|\gamma^i| + \lambda^i + \pi & \text{for negative one.} \end{cases} \tag{8}$$

For a cylindrical section, the equation parameters are:

$$\begin{aligned} q^i_{u,d^i} &= 0, \\ q^i_{v,d^i} &= -r^i\Delta\theta^i, \\ (\widehat{\boldsymbol{e}_{u,d^i}, \boldsymbol{w}^i}) &= \lambda^i. \end{aligned} \tag{9}$$

Details on the origin of the previous equations are given in 5.1.4. At step (2), only the conicity γ^i for conical sections

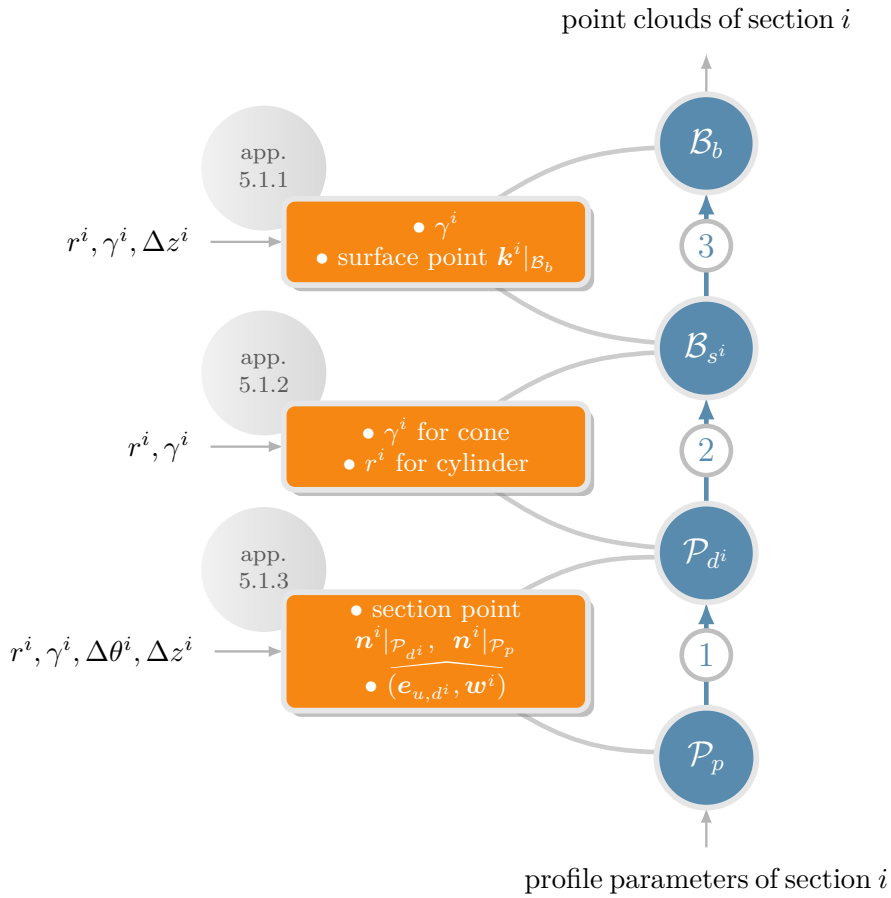

Figure 10. Steps for the stacking of a section i in $\mathcal{B}_b$ within `GEN` module, equation parameters (■) for the changes of bases.

and the radius r^i for cylindrical ones are required; these quantities are already known. Finally, at step (3), a point $\boldsymbol{k^i}|_{\mathcal{B}'_b}$ belonging to the wrapped surface of the section is required. The point $\boldsymbol{k^i}|_{\mathcal{B}'_b} = (r^i, 0, \Delta z^i)$ is chosen.

2.2.3 CAD model generation

The CAD model is computed with Salome in the basis $\mathcal{B}_b(\boldsymbol{q}^1)$ from the point clouds of all sections. The proposed methodology is inspired from a previously published tool [37], whose robustness has been strongly improved. For each section, the points of the suction side are interpolated with a cubic spline, as well as the points of the pressure side. Both splines are split in their middle; the contour of each section is thus described by four splines depicted with different colors in Fig. 11a. According to their relative position on the section, four groups of splines are created. From each group, a side face of the blade is generated by a spline approximation, see Fig. 11b. The degree of the approximation is automatically selected by Salome between 2 and 5 to respect a prescribed tolerance. The side faces (1), (2), (3) and (4) of the blade are thus generated to facilitate the subsequent computation of a regular mesh. The coincident edges are sewed to build a unique side surface and the holes at the hub and top of the blades are filled to generate the remaining faces. All faces are grouped in a unique shell, which is transformed in a volume. The resulting CAD model is shown in Fig. 11c.

The robustness of the sewing operation of side faces has been thoroughly assessed. For this operation, two faces are considered coincident on the basis of a prescribed tolerance. Providing a convenient estimation of this tolerance is not straightforward, as the four side faces are computed from four distinct approximations. An adaptive tolerance is introduced in the current work: the tolerance is initially defined by $\Delta z/200$, where Δz is the blade's width along

the $\boldsymbol{e}_{z,b}$ axis. If the sewing operation fails, the tolerance is doubled and a new sewing attempt is made, with a maximum of three attempts.

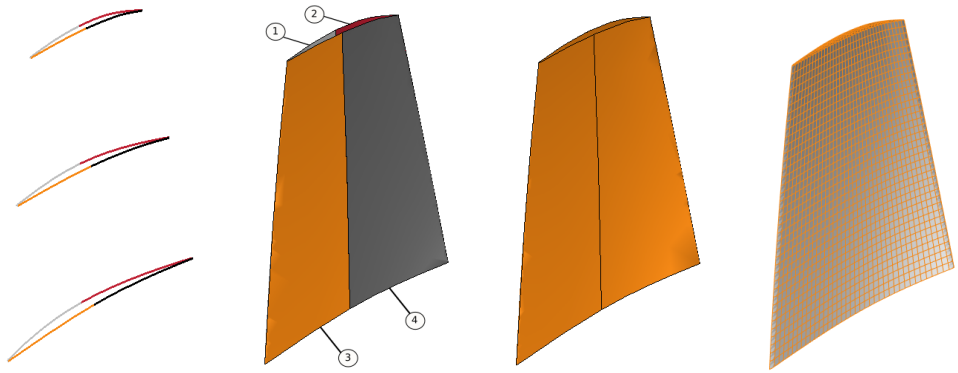

(a) section contours **(b)** side faces **(c)** CAD model **(d)** FE mesh

Figure 11. Steps to generate the CAD model (`GEN` module) and its FE mesh (`MSH` module).

2.2.4 FE discretization

The four edges spanning the blade height are discretized using n_h elements. For the sake of consistency, the same discretization is applied to the eight edges belonging to the hub and top faces. Quadrangle elements derived from the edges discretization are used to mesh the side faces whereas the hub and top faces are meshed with triangles. As a result, the complete volume is meshed with quadratic pentahedrons.

As the nonlinear dynamic simulations conducted on the blade are very sensitive to the submesh of the top face, the regularity of this submesh is thoroughly controlled: the areas of the triangles are limited by a fraction of the blade height. The FE mesh computed for the example with $n_\mathrm{h} = 38$ is made of 6384 elements and depicted in Fig. 11d. Based on the results of a thorough convergence analysis, not detailed here for the sake of brevity, this value is considered acceptable for the numerical simulations conducted in Sec. 4.

2.3 Parameter extraction (`PAR` module)

The aim of the `PAR` module is to extract the blade parameters from the input CAD blade model. It is assumed that the CAD model is provided in millimeters in a basis $\mathcal{B}_t$, that the blade rotates in the forward direction around the $(\boldsymbol{o}_t, \boldsymbol{e}_{z,t})$ axis and that the flow direction is $\boldsymbol{e}_{z,t}$. To position the blade in the blade basis $\mathcal{B}_b(\boldsymbol{q})$, the point $\boldsymbol{q}$ is chosen as the blade point with the smallest coordinate along $\boldsymbol{e}_{z,t}$. Should several points meet this criteria, the one with the smallest radius is chosen. The CAD model in $\mathcal{B}_b(\boldsymbol{q})$ is obtained by translation and rotation of the blade with respect to the $(\boldsymbol{o}_t, \boldsymbol{e}_{z,b})$ axis, so that the point $\boldsymbol{q}$ belongs to the $(\boldsymbol{o}_b, \boldsymbol{e}_{x,b})$ axis.

Sec. 2.3.1 describes the intersections of the CAD model with n_sec conical surfaces. The unwrapping of resulting sections and the stacking parameters identification are described in Sec. 2.3.2. The profiles parameters are then identified by solving an optimization problem detailed in Sec. 2.3.3. These steps are illustrated from the CAD model of rotor 37 intersected with $n_\mathrm{sec} = 3$ surfaces, see Fig. 12. For this model, the point $\boldsymbol{q}$ belongs to the leading edge of the hub face of the blade.

2.3.1 Intersection of the blade with the conical surfaces

The conical surface of section $i \in \{1, ..., n_\mathrm{sec}\}$ is defined by the conicity parameter γ^i. A point $\boldsymbol{m}$ belonging to this surface satisfies the following equation:

$$m_{r,b} = m_{z,b} \tan(\gamma^i) + b^i, \tag{10}$$

where $b^i > 0$ is the radius of the surface in the plane $(\boldsymbol{o}_b, \boldsymbol{e}_{r,b}, \boldsymbol{e}_{\theta,b})$. The quantities γ^i and b^i are then sufficient to generate the surface i. The conical surfaces are equally distributed along the blade height such that:

$$\gamma^i = \gamma^1 + (\gamma^{n_{\text{sec}}} - \gamma^1)\frac{i-1}{n_{\text{sec}}-1} \quad \forall i \in \{1, ..., n_{\text{sec}}\}, \tag{11}$$

$$b^i = b^1 + (b^{n_{\text{sec}}} - b^1)\frac{i-1}{n_{\text{sec}}-1} \quad \forall i \in \{1, ..., n_{\text{sec}}\}. \tag{12}$$

Consequently, only the quantities $\gamma^1, b^1, \gamma^{n_{\text{sec}}}$ and $b^{n_{\text{sec}}}$ related to the hub and top sections are required to generate all the conical surfaces. The computation of these quantities is semi-automatized: a coarse mesh of the blade is generated and several nodes on the top and hub faces are selected by the user. Surface parameters related to each face are computed from a distinct linear regression conducted to fit Eq. (10) to the selected face points. The blade is then intersected by each of the n_{sec} conical surfaces, see Fig. 12. The contour of the resulting sections are finely discretized and stored as n_{sec} point clouds.

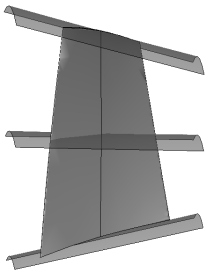

Figure 12. Intersection of the CAD model of rotor 37 with $n_{\text{sec}} = 3$ conical surfaces.

2.3.2 Identification of the stacking parameters

Among the stacking parameters listed in Table 1, only the conicity parameter γ^i is known at this point from Eq. (11). The coordinates of the point $\boldsymbol{q}^i|_{\mathcal{B}_b}$ are required to compute the other parameters. In order to prevent numerical errors and ensure consistency with the blade generation described in Fig. 10, this point must be identified in the profiles basis $\mathcal{P}_p$.

The point cloud of each section is projected from basis $\mathcal{B}_b$ to basis $\mathcal{P}_p$, see steps (1), (2) and (3) in Fig. 13. The point $\boldsymbol{q}^i|_{\mathcal{P}_p}$ is computed and this point is then projected from basis $\mathcal{P}_p$ to $\mathcal{B}_b$ during steps (4), (5) and (6). The intermediate coordinates $\boldsymbol{q}^i|_{\mathcal{P}_{d^i}}$ are used to compute the setting angle λ^i from Eq. (5). Once the points $\boldsymbol{q}^i|_{\mathcal{B}_b}$ of all sections $i \in \{1, ..., n_{\text{sec}}\}$ are known, the parameters $r^i, \Delta\theta^i$ and Δz_i are computed from Eq. (1), (2) and (3).

The computation of equations parameters is detailed hereafter. At step (1), the point $\boldsymbol{k^i}$ belonging to the surface is chosen such that $\boldsymbol{k}^i|_{\mathcal{B}'_b} = (b^i, 0, 0)$, according to Eq. (10). At step (2), the radius r^i of cylindrical section is given by the quantity b^i defined in Eq. (12). At step (3), the point $\boldsymbol{n}^i$ is chosen such that $\boldsymbol{n}^i = \boldsymbol{a}^i$; the coordinates $\boldsymbol{a}^i|_{\mathcal{P}_p}$ are known by definition as $\boldsymbol{a}^i|_{\mathcal{P}_p} = \boldsymbol{o}_p$. To determine the point $\boldsymbol{a}^i|_{\mathcal{P}_{d^i}}$, the camber line of the profile is computed by a fifth degree polynomial approximation of the section point cloud. The section point $\boldsymbol{a}^i|_{\mathcal{P}_{d^i}}$ is chosen as the point the nearest of the camber line on the leading edge. The point $\boldsymbol{b}^i$ required to compute the chord vector $\boldsymbol{w}^i$ defined in Eq. (4) is chosen as the section point the most remote from $\boldsymbol{a}^i$.

2.3.3 Identification of the profile parameters

Let N^i be the target profile computed by sampling with approximately 200 points the point clouds of the profile i in $\mathcal{P}_p$. The target profile N^1 of the hub section of rotor 37 is presented in Fig. 14. The profile parameters describing a

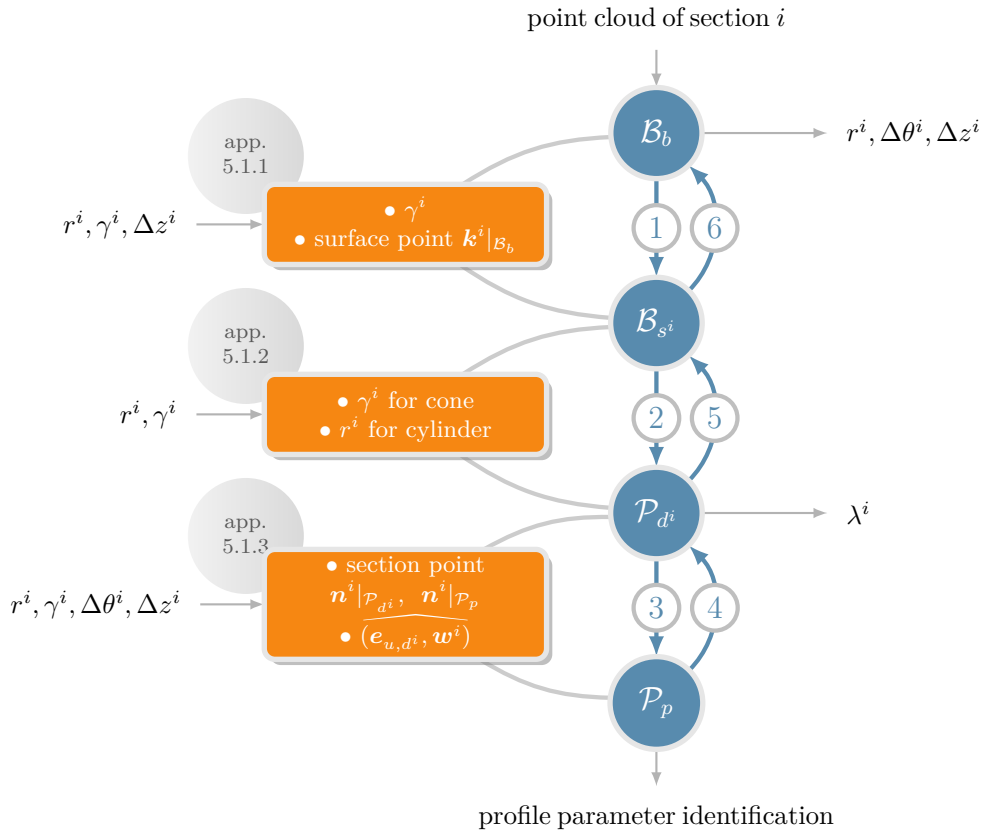

Figure 13. Steps for the identification of stacking parameters in `PAR`, equation parameters (■).

target profile are identified by solving the following optimization problem:

$$\begin{aligned} &\min_{\boldsymbol{x}} e(\boldsymbol{x}) \\ &\boldsymbol{l} \leq \boldsymbol{x} \leq \boldsymbol{u}, \end{aligned} \tag{13}$$

where $\boldsymbol{x} \in \mathbb{R}^{14}$ is the vector of profile parameters, $\boldsymbol{l}, \boldsymbol{u} \in \mathbb{R}^{14}$ are bound vectors and $e(\boldsymbol{x})$ is an error function quantifying the differences between the target profile and the parameterized profile defined by $\boldsymbol{x}$. The definition of the objective function $e(\boldsymbol{x})$, proposed in a previous work [38], is recalled:

$$e(\boldsymbol{x}) = 0.9\bar{d}(\boldsymbol{x}) + 0.1|\delta p(\boldsymbol{x})|, \tag{14}$$

where $\bar{d}(\boldsymbol{x})$ is the average distance between the points of the cloud N^i and the parameterized profile and $\delta p(\boldsymbol{x})$ is the relative perimeter difference between profiles.

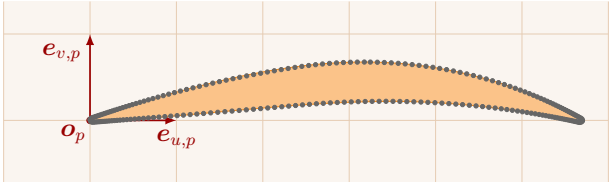

Figure 14. Target profile (●) and parameterized profile (■) with $e(\boldsymbol{x}) \simeq 0.22$ for the hub section of rotor 37.

For each set of profile parameters $\boldsymbol{x}$ satisfying $\delta p(\boldsymbol{x}) \neq 0$, the objective function is differentiable. However, the gradient is not known analytically because of the discretization of the profiles and additional efforts would be required to compute it. As a consequence, Problem (13) is treated as a derivative-free problem and solved with NOMAD software v.3.9.1 [39] based on the Mads algorithm [36]. A vector of initial parameters $\boldsymbol{x}^0$ is required to start the optimization process. These parameters are computed from the coordinates of points of N^i, see Fig. 15 and Table 2. To improve the robustness of the parameters identification, the bounds vectors of Problem (13), given in Table 2, are relative to target profile N^i as well. The camber line $g^i(m_{u,p}) : \mathbb{R} \to \mathbb{R}$ of the profile is required and computed from a fifth degree polynomial approximation of the section point cloud. The optimal coordinates of the suction point $(s^i_{u,p}, s^i_{v,p})$ and the chord c^i are directly computed from the target profile and thus kept constant in the optimization process. The dimension of Problem (13) is then reduced to 11.

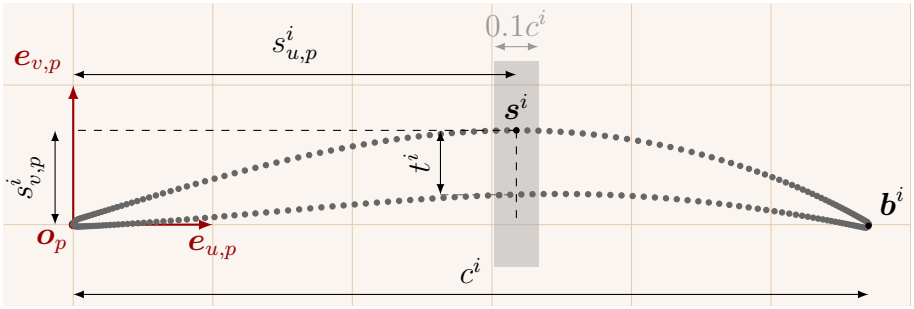

(a) suction point coordinates, chord and thickness

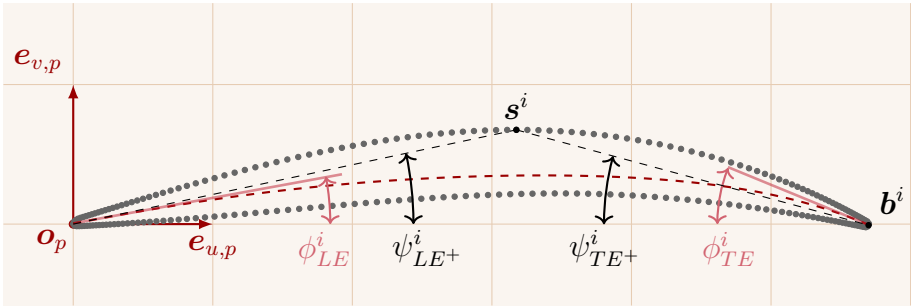

(b) inlet, outlet and upper wegde angles

Figure 15. Initial profile parameters from the target profile (●) and camber line $g(m_{u,p})$ (- - -).

Problem (13) is solved with the default parameters of NOMAD with a budget of 1500 evaluations of $e(x)$. The parameterized profile obtained for the hub section of rotor 37 is shown in Fig. 14. The asymptotic convergence of the algorithm was checked on 17 profiles of rotor 37 and results show that 1500 evaluations are sufficient to converge to low error values.

2.4 Partial conclusion

Recent blade parameterizations used for aerodynamic studies ensure that the side surface of the blade has continuous curvature, which corresponds to a $\mathcal{G}^2$ regularity constraint. Indeed, curvature discontinuities may induce velocity peak and flow separation phenomena [40]. Although the present work focuses on considerations only, details on the regularity of the profile parameterization and the CAD model are given hereafter:

profiles $\mathcal{G}^1$: the seven curves depicted in Fig. 9 used to draw a profile in $\mathcal{P}_p$ are $\mathcal{G}^\infty$. As the tangents are preserved at the intersections of curves, the whole profile is a $\mathcal{G}^1$ curve. Actually, it can be shown that the profile is $\mathcal{G}^2$ except at points $\boldsymbol{s}^i$ and $\boldsymbol{p}^i$. The continuity of the curvature direction at these points may be ensured by using fifth degree splines for curves (3), (4), (5) and (6). However, the $\mathcal{G}^2$ constraint was found to strongly limit the shapes allowed by the parameterization. In the context of this study, the choice was made to force only $\mathcal{G}^1$

Table 2. Initial parameters and bounds for the identification problem.

parameter	$\boldsymbol{x}^0$	$\boldsymbol{l}$	$\boldsymbol{u}$
$s^i_{u,p}$	$m_{u,p} : \boldsymbol{m} \in \arg\max_{\boldsymbol{m}\in N^i} m_{v,p}$	—	—
$s^i_{v,p}$	$\max_{\boldsymbol{m}\in N^i} m_{v,p}$	—	—
$p^i_{v,p}$	$c^i/2$	0	c^i
c^i	$\max_{\boldsymbol{m}\in N^i} m_{u,p}$	—	—
t^i	$s^i_{v,p} - \min_{\boldsymbol{m}\in N^i}\{m_{v,p} : \lvert m_{u,p} - s_{u,p}\rvert < 0.05c^i\}$	$c^i/100$	$c^i/2$
$r^i_{LE^+}$	$t^i/5$	$t^i/50$	t^i
$r^i_{LE^-}$	$t^i/10$	$t^i/50$	t^i
r^i_{TE}	$t^i/10$	$t^i/100$	t^i
ϕ^i_{LE}	$\arctan(g'(0))$	0°	90°
$\psi^i_{LE^+}$	$\arctan(s^i_{v,p}/s^i_{u,p})$	0°	89°
$\psi^i_{LE^-}$	$\psi^i_{LE^+}$	0°	89°
ϕ^i_{TE}	$\arctan(-g'(b^i_{u,p}))$	0°	90°
$\psi^i_{TE^+}$	$\arctan(s^i_{v,p}/(c^i - s^i_{u,p}))$	0°	89°
$\psi^i_{TE^-}$	$\psi^i_{TE^+}$	0°	89°

regularity to ensure the fidelity of parameterized models. Nonetheless, the $\mathcal{G}^2$ regularity is achieved for the side surface of the blade.

side surface of CAD model $\mathcal{G}^2$ To generate the CAD model, each profile is discretized and the resulting point cloud is projected from $\mathcal{P}_p$ to $\mathcal{B}_b$. Pressure and suction sides of the section are computed by cubic splines; they are thus $\mathcal{G}^2$. Considering that the point cloud is sufficiently dense, as the $\mathcal{G}^2$ regularity is preserved by the conical transform from $\mathcal{P}_p$ to $\mathcal{B}_b$, then the section contour in $\mathcal{B}_b$ is $\mathcal{G}^2$ at leading and trailing edges. Consequently, all section contours are $\mathcal{G}^2$. The four side faces of the CAD model are spline approximations of class $\mathcal{G}^\infty$. Thus, the regularity of the whole side surface at the face intersections depends on the regularity of the section contours. The side surface of the CAD model is thus $\mathcal{G}^2$ at the intersection of faces. This characteristic was checked numerically.

3 Validation on NASA's rotor 37 and rotor 67

The proposed methodology is validated with respect to its robustness, numerical efficiency and fidelity. The first two aspects are detailed in 5.4. This section focuses on the fidelity assessment: specific criteria are introduced to compare the parameterized blade model with the input blade. In published redesign processes, the assessment of the fidelity of parameterized blades may not be addressed when an approximate model is acceptable [13]. Most of the time, geometric comparison criteria are used to quantify the similarity between the CAD models globally [15, 19, 22, 23] or locally, at the profile level [10, 14, 18, 23]. These criteria are computed by commercial software packages and underlying equations are often not detailed. While the need for criteria going beyond geometrical considerations—such as aerodynamic, manufacturing or dynamic properties—has been recently underlined [12], such criteria are still rarely used [8].

In the present work, the fidelity of parameterized blades is thoroughly assessed based on both geometric and dynamic criteria. While the use of geometrical criteria is natural with respect to the literature, they only provide a raw comparison of the geometries. As they are not sufficient to quantify the differences in dynamic behaviors, which are of primary interest in the context of contact interactions, dynamic criteria are considered to bring a complementary insight on the required fidelity level.

The validation is conducted on the compressor blade NASA rotor 37 and fan blade NASA rotor 67. From

the input CAD models—freely available online[4]—the `PAR` and `GEN` modules are successively used to extract blade parameters and to generate the parameterized CAD models.

The comparison criteria are analyzed with respect to the number of sections n_{sec}. This parameter is supposed to have a strong impact on the fidelity of parameterized blades, as a minimal number of sections is required to accurately capture the blade curvature. The values of other parameters related to the parameter extraction, such as the discretization of curves and the formulation of the identification problem, are taken from previous works or have been determined empirically. The parameterized models are computed for $n_{\text{sec}} \in \{2, 3, 5, 9, 17\}$ in a dichotomous manner.

3.1 Geometric criteria

The parameterized CAD models obtained for rotor 67 for $n_{\text{sec}} \in \{2, 3\}$ are pictured in Fig. 16. At least 3 sections are required to accurately represent the blade curvature. For $n_{\text{sec}} \geq 3$, a visual inspection of the CAD models does not reveal any discrepancy between them. Two geometric comparison criteria are used: a criterion related to the CAD model volumes is introduced in the first subsection and a local criterion based on profile similarity is described in the second subsection.

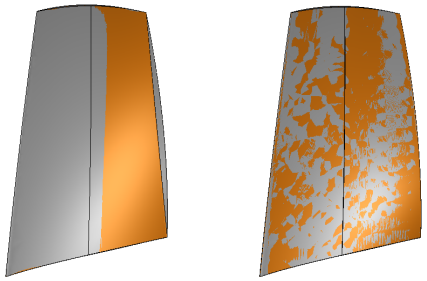

(a) $n_{\text{sec}} = 2$ **(b)** $n_{\text{sec}} = 3$

Figure 16. Input (■) and parameterized (■) CAD models of rotor 67.

3.1.1 Blade volume

The volume V of the input CAD model is divided into two parts depicted in Fig. 17: the inner volume V_{in}, between the top and hub conical surfaces, and the outer volume V_{out}, beyond these surfaces. The outer volume proportion ΔV_{out} and the inner volume variation ΔV_{in} of a parameterized CAD model with respect to the input one are defined by:

$$\Delta V_{\text{out}} = \frac{V_{out}}{V} \times 100 \quad [\%] \qquad \Delta V_{in} = \frac{V'_{\text{in}} - V_{\text{in}}}{V_{\text{in}}} \times 100 \quad [\%],$$

where V'_{in} is the inner volume of the parameterized CAD model. The volumes variations are presented in Table 3.

Table 3. Volume variations of the parameterized CAD models for rotor 37 and rotor 67.

blade	ΔV_{out} [%]	ΔV_{in} [%]				
		$n_{\text{sec}} = 2$	$n_{\text{sec}} = 3$	$n_{\text{sec}} = 5$	$n_{\text{sec}} = 9$	$n_{\text{sec}} = 17$
rotor 37	0.12	-0.5	1.04	0.79	0.96	0.81
rotor 67	neg.	-10.04	-0.1	-0.1	-0.8	0.25

[4] `https://lava-wiki.meca.polymtl.ca/public/modeles/accueil`

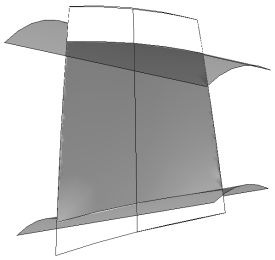

Figure 17. Blade volume partition: outer volume V_{out} (□) (exaggerated), inner volume V_{in}(■).

For rotor 67, the outer volume V_{out} cannot be computed with Salome because the conical surfaces are too close of the blade tip and hub faces. The quantity ΔV_{out} is thus considered negligible. For rotor 37, only 0.12 % of the volume of the input blade is lost. The proposed methodology thus yield a negligible volume loss a the top and hub of the studied blades. The inner volume V_{in} varies with respect to n_{sec} for both blades. With $n_{\text{sec}} = 2$, the volume of the input blade is greater than the volume of the parameterized blade because the side surface of the blade is generated by a linear interpolation in this case. Increasing n_{sec} up to 5 makes it possible to more accurately represent the blade curvature; the inner volume variation with $n_{\text{sec}} = 5$ represents only 0.1 % for rotor 67 and 0.79 % for rotor 37. For $n_{\text{sec}} \geq 5$, the quantity ΔV_{in} stays small but slightly fluctuates with the value of n_{sec}. This is assumed to be related to the accumulation of local errors on the additional sections at the profile scale.

3.1.2 Profile shape

The similarity between a parameterized profile, defined by a parameter vector $\boldsymbol{x}$, and a target profile N^i is quantified by the error function $e(\boldsymbol{x})$ defined in Eq. (14). According to previous work based on plane sections [38, p. 35], a target profile is considered well-represented if $e(\boldsymbol{x}) \leq 0.05$ for a model provided in millimeters. The use of conical surfaces implies a deformation of sections from basis $\mathcal{B}_b$ to $\mathcal{P}_p$. The parameterization proposed in the current work is validated hereafter for profiles lying on conical surfaces.

For rotor 37 and rotor 67, the profile parameters vectors identified for the 17 sections all satisfy $e(\boldsymbol{x}) < 0.05$. According to the error function values, these profiles issued from conical sections are correctly represented with the proposed parameterization. This also attests of the fidelity of the procedure for a variety of profile shapes. The parameterized profiles of the hub section of rotor 37 and rotor 67 and shown in Fig. 14 and Fig. 18.

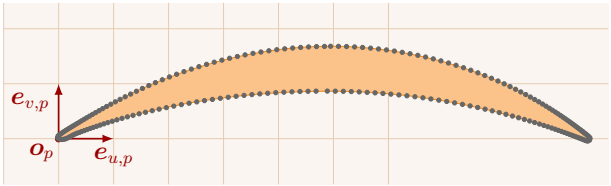

Figure 18. Target profile (●) and parameterized profile (■) for the hub section of rotor 67.

3.2 Dynamic criteria

Contact interactions are particularly sensitive to small variations of the geometry, especially lean or sweep variations defining the stacking of blade sections [32]. Indeed, in a highly nonlinear context, small geometrical errors may lead to unacceptable differences in dynamic behaviors. As a consequence, the fidelity of the parameterized model must be high enough not to introduce changes in the blade's dynamic response comparable to those obtained in the literature due to deliberate modifications of the blade parameters. Comparison criteria related to the blade dynamics are thus required to assess the fidelity of the parameterized model in the context of contact interactions.

Three dynamic criteria are considered. An accurate representation of natural frequencies is essential to finely represent the blade vibratory response. Consequently, in the first subsection, a criteria quantifying the errors on

natural frequencies between the input blade and parameterized blades is introduced. A quantitative criteria based on the dynamic clearance of the blades—which is assumed to be a relevant quantity to look at in order to assess a blade's robustness to contact [20, 32, 41]— is introduced in the second subsection. The third subsection deals with the qualitative comparison of Nonlinear Frequency Response Curves (NFRC), obtained from simulations predicting the vibration response of the blades undergoing contact interactions.

The computation of these criteria requires FE meshes of the input and parameterized blades, which are computed with the `MSH` module. According to convergence studies, the number of elements along the radial direction of the blade is fixed to $n_{\mathrm{h}} = 38$, which leads to FE meshes of 6384 (respectively 6232) elements for rotor 37 (respectively 67) models. As the FE meshes have high influence on the dynamic criteria, the input blades have been meshed manually with the `MSH` module. This way, it is ensured that all FE meshes related to a specific blade share the same number of elements and topology.

3.2.1 Natural frequencies

The relative error on the jth natural frequency of a parameterized blade with respect to the input one is defined by:

$$\Delta f_j = \frac{|f'_j - f_j|}{f_j} \times 100 \quad [\%],$$

where f_j (respectively f'_j) is the jth natural frequency of the input (respectively parameterized) blade. The natural frequency errors are only computed for the first modes $j \in \{1, ..., 10\}$. Indeed, the influence of higher order modes is supposed to be negligible on the dynamics of the studied blades. As the first mode of rotor 37 and rotor 67 is a bending mode likely to cause structural contact/interactions, a maximal variation of 1 % is targeted for this mode.

The natural frequency errors for rotor 37 and rotor 67 models are given in Fig. 19. The results shown for models with $n_{\mathrm{sec}} \geq 3$ demonstrate an excellent agreement on the natural frequencies. The errors diminish for most frequencies by increasing n_{sec} up to 5. For $n_{\mathrm{sec}} \in \{9, 17\}$, the errors remain low but are slightly higher than those computed for $n_{\mathrm{sec}} = 5$ for both blades. This may be explained by the accumulation of errors on profiles. For both blades, the lowest error are obtained for $n_{\mathrm{sec}} = 5$: all errors are less than 2 % for rotor 37 and 1 % for rotor 67. The error on the first natural frequencies are less than 0.6 % for rotor 37 and 0.08 % for rotor 67. The orders of magnitude of these errors are similar to those observed after slight changes of the number of finite mesh elements in convergence studies. The fidelity with respect to natural frequencies is thus considered excellent for these models. It is also noticeable that the errors on natural frequencies are coherent with the volume variations observed in Table 3: smaller frequencies errors are observed for smaller volume variations.

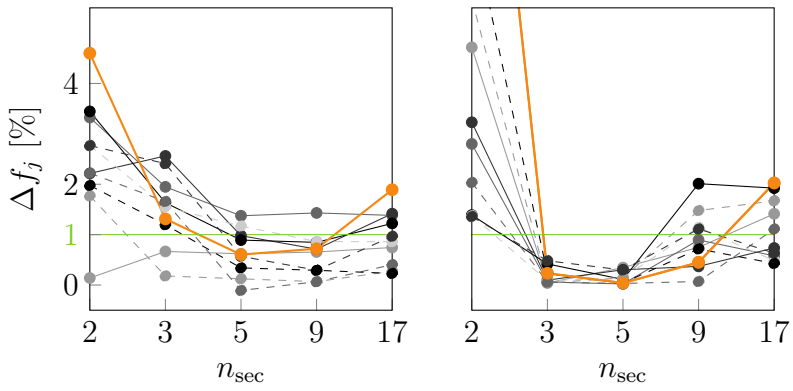

(a) rotor 37 **(b)** rotor 67

Figure 19. Natural frequencies errors between parameterized blades and input blade: Δf_1 (—●—), Δf_2 (—●—), Δf_3 (—●—), Δf_4 (—●—) , Δf_5 (—●—), Δf_6 (- ●-), Δf_7 (- ●-), Δf_8 (- ●-), Δf_9 (- ●-), Δf_{10} (- ●-).

3.2.2 Dynamic clearance

The dynamic clearance represents the clearance variation between a blade and its surrounding casing as the blade vibrates along one of its free-vibration modes [20]. In the present work, the dynamic clearance c_d associated to the first bending mode of a blade is computed for the node $\boldsymbol{u}$ at its leading edge. More specifically, a single scalar value c_{d,u^*} is considered, corresponding to the minimal blade-tip/casing clearance as the tangential displacement of the blade's leading edge is $u_{b,y} = u^* = \pm 2$ mm. The relative error on the dynamic clearance c_{d,u^*} of a parameterized blade with respect to the input one is defined by:

$$\Delta c_{d,u^*} = \frac{c'_{d,u^*} - c_{d,u^*}}{c_{d,u^*}} \times 100 \quad [\%],$$

where c_{d,u^*} (respectively c'_{d,u^*}) is the dynamic clearance computed for the input (respectively parameterized) blade.

The errors on dynamic clearances computed for rotor 37 and rotor 67 are depicted in Table 4. For models with $n_{\text{sec}} \geq 3$, the agreement between the input model and the parameterized model is excellent. In particular, models with $n_{\text{sec}} = 5$ exhibit the lowest errors for both blades. The evolution of errors with respect to n_{sec} is coherent with the evolution of volume variations observed in Table 3.

Table 4. Dynamic clearance errors between parameterized blades and input blade.

blade	$\boldsymbol{\Delta c_{d,u^*}}$ [%]				
	$n_{\text{sec}} = 2$	$n_{\text{sec}} = 3$	$n_{\text{sec}} = 5$	$n_{\text{sec}} = 9$	$n_{\text{sec}} = 17$
rotor 37	6.23	0.24	-0.09	-0.14	0.27
rotor 67	-22.08	-1.03	-0.94	-0.94	-3.72

3.2.3 Vibration response to contact

A published numerical strategy based on time integration [42] is used to predict the vibration responses of rotor 37 and rotor 67 blades for a large range of angular speeds ω considering a contact scenario featuring a rigid ovalized casing. Simulation parameters are given in 5.3. The simulations are conducted on Craig-Bampton reduced-order models [43] of the full FE meshes for the sake of efficacy. Eight boundary nodes evenly distributed along the blade-tip are retained for contact management. These nodes are the same for all FE meshes related to a blade in order to ensure consistent numerical simulations.

For both rotor 37 and rotor 67, the results obtained for the parameterized models with $n_{\text{sec}} \in \{3, 5, 9\}$ are compared to those of the input blades. The NFRC of each model is computed from the infinite norm of the global displacement $\boldsymbol{d}_{LE}$ of the leading edge boundary node over the last blade revolution. The NFRC are superimposed for each blade in Fig. 20. The criterion considered in this section accounts for the quantitative comparison of displacement magnitudes and the qualitative comparison of the nature of the computed solutions. This criterion is particularly strict: considering the nonlinear phenomena involved in contact simulations, *e.g.* bifurcations [44] or coexistent solutions on large speed range, as well as the use of a time solver, a small variation between parameterized and input blades could indeed lead to very different vibration responses.

The agreement between the NFRC of the input and parameterized models, depicted in Fig. 20, is excellent for both blades. A minor shift in angular speed is visible for parameterized models, for instance between 1490 and 1530 rad·s^{-1} for rotor 37. This is related to the small natural frequencies errors observed between the parameterized and input blades. For speed ranges where the computed solutions are periodic for the input blade, e.g. between 1200 and 1250 rad·s^{-1} for rotor 67, the analysis of time signals reveal periodic solutions for parameterized models as well. Time displacements on the last period were compared and excellent agreement was found. On other angular speed ranges, e.g. around 1300 rad·s^{-1} for rotor 67, point clouds reveal the presence of coexistent solutions. These zones are located on similar speed ranges for all NFRC related to a blade. From a qualitative viewpoint, the nature of the solutions is thus preserved with parameterized models. Besides, the good superimposition of the NFRC of each blade demonstrates the fidelity of parameterized models for all considered values of n_{sec}. This also supports

the idea that the slight differences observed between input and parameterized models are likely to be caused by the limits of the profile parameterization.

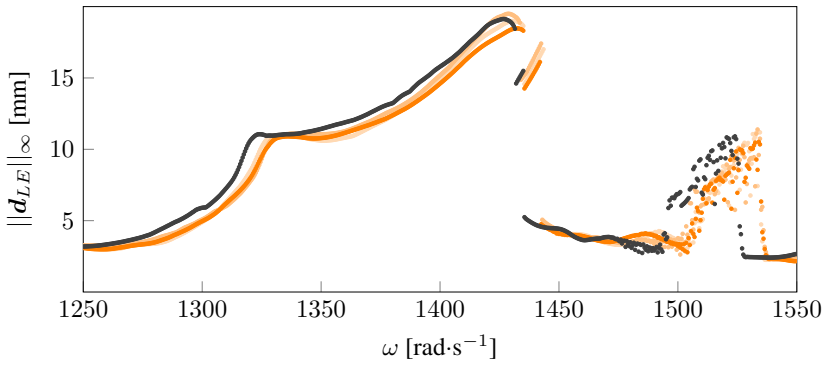

(a) rotor 37

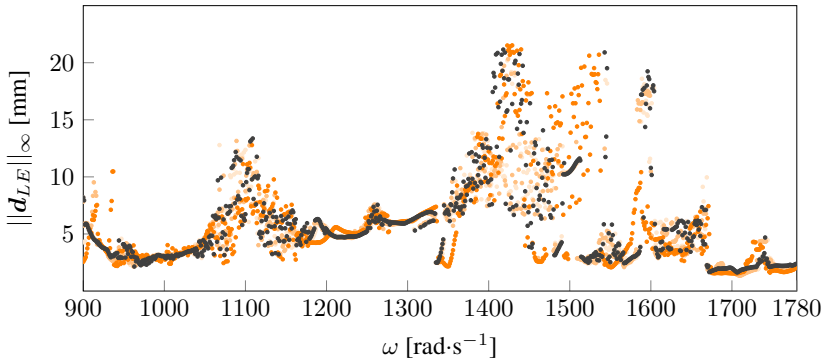

(b) rotor 67

Figure 20. NFRC of input (●) and parameterized blades with $n_{\text{sec}} = 3$ (●), $n_{\text{sec}} = 5$ (●) and $n_{\text{sec}} = 9$ (●).

3.3 Validation outcome

For both rotor 37 and rotor 67, parameterized CAD models with $n_{\text{sec}} \geq 3$ are visually indistinguishable from the input model. A good agreement in geometrical criteria was observed for parameterized models with $n_{\text{sec}} \geq 3$. In particular, the volume loss resulting from the intersection of blades with the conical surfaces is negligible. In terms of dynamic criteria, the models with $n_{\text{sec}} \in \{3, 5, 9\}$ exhibit excellent results. The best compromise for all studied criteria are obtained with the 5-section model and demonstrate the high fidelity of this model considering both geometric and dynamic aspects. Besides, the similarity between the values obtained for different number of sections attests of the stability of the developed tool with respect to n_{sec}.

4 Redesign of NASA rotor 37

The applicability of the developed two-way modelling method within the complete redesign process depicted in Fig. 1 is assessed on the input blade rotor 37. A high fidelity parameterized model of the blade is computed with the `PAR` module and called initial blade. This initial blade is used as starting point of the iterative update step presented in Sec. 4.1 and the performance check of the optimized blade is described in Sec. 4.2.

4.1 Update of the initial blade

Because it was shown to be the closest to the input blade, the 5-section parameterized model of rotor 37 is chosen as the initial blade. The update of the blade relies on an optimization problem: some blade parameters, chosen as

optimization variables, are allowed to be modified in order to improve a performance criterion related to the blade robustness with respect to contact interactions.

In order to efficiently assess the blade robustness, the dynamic clearance is used as surrogate, *i.e.* a quantity assumed to provide a computationally inexpensive estimate of the blade robustness to contact [20]. The dynamic clearance is computed for the first bending mode, for which specific structural interactions have been reported along the fourth engine order [31]. The performance criterion considered for the update step is thus the dynamic clearance c_{d,u^*} introduced in Sec. 3.2.2.

To ensure the numerical efficiency of the optimization process, only a few parameters are chosen as optimization variables. The profile parameters are kept identical to the initial blade to preserve industrial aerodynamic properties. As the influence of lean angle and sweep distance on contact robustness have been shown in a previous work [32], only the stacking parameters $\Delta\theta^i$ and Δz^i are allowed to vary. According to Eq. (2) and (3), the hub quantities $\Delta\theta^1$ and Δz^1 are null by definition. For each profile generated during the update, in order to ensure that realistic blade shapes are generated, lean angles and sweep distance of sections 2 and 4 are computed by means of a quadratic interpolation of the values at sections 1, 3 and 5. The vector of optimization variables is thus defined as $\boldsymbol{x} = \{\Delta z^3, \Delta\theta^3, \Delta z^5, \Delta\theta^5\}$ and all blade parameters $\boldsymbol{y}$ may be computed by a mapping function $m(\boldsymbol{x})$ according to the previous choices.

The 4-variable optimization problem solved during the update phase is thus formulated as:

$$\begin{aligned} &\max_{\boldsymbol{x}} c_{d,u^*}(m(\boldsymbol{x})) \\ &\quad \boldsymbol{l} \leq \boldsymbol{x} \leq \boldsymbol{u}, \end{aligned} \tag{15}$$

where $c_{d,u^*}(m(\boldsymbol{x}))$ is the dynamic clearance associated to the blade parameters $y = m(\boldsymbol{x})$ and $\boldsymbol{l}$,$\boldsymbol{u} \in \mathbb{R}^4$ are bound vectors defined in Table 5. For a given vector $\boldsymbol{y}$, the simulation time required to compute the quantity $c_{d,u^*}(\boldsymbol{y})$ is approximately 30 seconds on a standard PC. Besides, the gradient of the dynamic clearance is not available. Problem (15) is thus considered as a blackbox optimization problem and solved with the Mads algorithm [36]. This algorithm is well-suited for time-consuming simulations and can manage failed simulations without stopping the optimization. The default parameters of NOMAD v.3.9.1 are used and 400 simulations of the dynamic clearance are allowed. The initial dynamic clearance value $c_{d,u^*}(\boldsymbol{y}^0)$ is approximately -0.46 mm, see Fig. 21. From the optimized

Table 5. Bounds of the optimization problem.

optimization variables	$\boldsymbol{l}$	$\boldsymbol{u}$
Δz^3, Δz^5 [mm]	-2	$+2$
$\Delta\theta^3$, $\Delta\theta^5$ [°]	-1.5	$+1.5$

vector $\boldsymbol{x}^*$ returned by the algorithm, the optimized blade parameters $\boldsymbol{y}^* = m(\boldsymbol{x}^*)$ lead to a dynamic clearance of -0.0089 mm, which represents an improvement of 98 % with respect to the initial dynamic clearance. Initial and optimized CAD models are depicted in Fig. 22: the optimized blade shape is realistic and presents a strong variation of the lean angle from backward to forward direction along the blade height, see Fig. 22a. The sweep distance follows the same trend, as shown in Fig. 22b. During the optimization process, only 3 simulations out of 400 failed because of errors in the CAD or mesh generation, which attests of the robustness of the developed tool.

4.2 Performance check of the updated blade

The dynamic clearance c_d of the initial and optimized blades are computed for tangential displacements $u_{b,y} = \pm 2$ mm and plotted in Fig. 21. The slope of the curves quantifies the evolution of the dynamic clearance when the blade vibrates along the first bending mode. A significant decrease in the curve slope may be observed for the optimized blade: for a same tangential displacement, the dynamic clearance varies much less.

Numerical simulations are conducted to predict the vibration response of the optimized blade to the contact scenario described in Sec. 3.2.3. The global displacement vectors of the leading and trailing edges boundary nodes over the last blade revolution, denoted $\boldsymbol{d}_{LE}$ and $\boldsymbol{d}_{TE}$, are used to compute the NFRC depicted in Fig. 23. One may note that the magnitude of displacements predicted for the initial blade around the nonlinear resonance are far

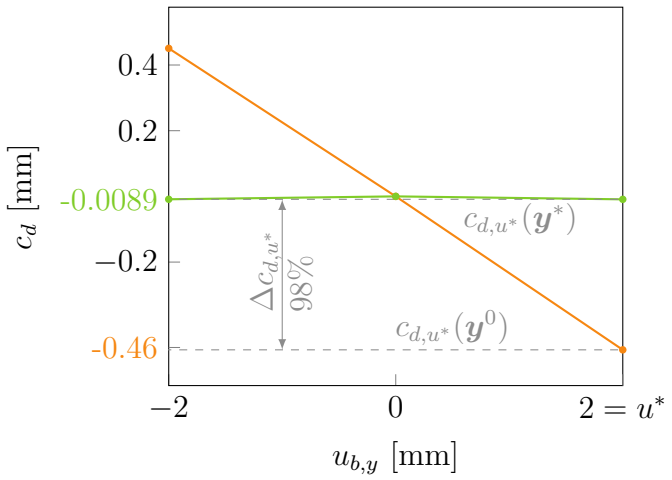

Figure 21. Dynamic clearances curves with respect to tangential displacement for initial (—) and optimized (—) blades.

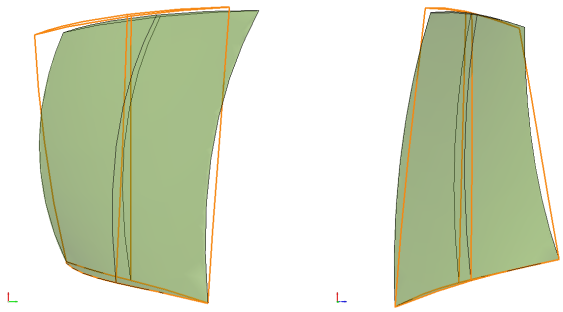

(a) $(\boldsymbol{o}_b, \boldsymbol{e}_{x,b}, \boldsymbol{e}_{y,b})$ plane **(b)** $(\boldsymbol{o}_b, \boldsymbol{e}_{x,b}, \boldsymbol{e}_{z,b})$ plane

Figure 22. CAD models of initial (□) and optimized (□) blade.

above acceptable values for a linear FE model. The numerical model suggests that plastic deformations, potentially cracks, will occur. This is a clear indication of the severity of the considered contact configuration. In this context, the reduction by 75 % of the maximum amplitude of displacement observed for the optimized blade is remarkable. It underlines that the optimized blade is predicted to be far more robust than the initial blade to the simulated interaction.

In order to get a deeper understanding of the differences between the initial and optimized blades, the NFRC related to displacements along $\boldsymbol{e}_{x,b}, \boldsymbol{e}_{y,b}$ and $\boldsymbol{e}_{z,b}$ directions are plotted in Fig. 24. For comparison purposes, the previous NFRC related to global displacements are shown in gray in the background. Amplitudes of vibration are reduced in all directions throughout the considered angular speed range.

The developed modelling tool is fully integrated in the redesign process and its robustness, resolution and computational efficiency allow for a successful redesign of rotor 37. Besides, the relevance of the dynamic clearance as a design criterion to account for robustness to contact interactions is again underlined and in agreement with previous publications. An extension of this criterion to other low frequency free vibration modes—such as the first torsion mode—could broaden the scope of optimization to larger angular speed ranges in order to mitigate other types of interactions.

The modularity of the proposed methodology allows to account for other criteria, including aerodynamic performance. While a realistic blade design must account for aerodynamic considerations, it is here demonstrated that optimization based on structural aspects only yields significant improvements with respect to its dynamics

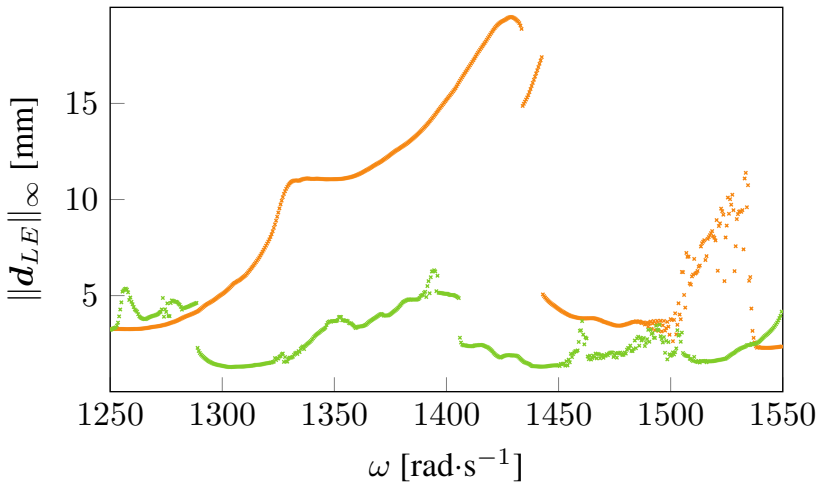

(a) LE

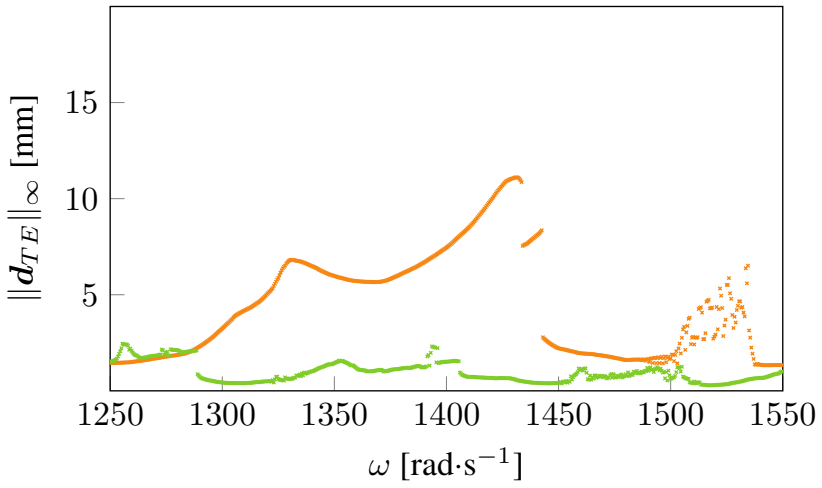

(b) TE

Figure 23. NFRC of LE and TE displacements for initial (—) and optimized (—) blades.

response. Presented results thus underline the need to find a new balance between aerodynamics and structural dynamics in blade design process.

5 Conclusion

This work proposes an original two-way modelling method to parameterize existing blades and generate CAD models from blade parameters. The method is embedded in a numerical tool fully integrated in the first redesign process of blades more robust to contact interactions. Attention is paid to the fidelity assessment of parameterized models with respect to input blades. This assessment goes beyond the usual comparison of geometric CAD models and encompasses mechanical criteria related to blade vibrations. The validation is conducted for NASA rotor 37 and rotor 67 blades whose geometries are very different; an excellent agreement is observed between initial and parameterized models. The applicability of the developed modelling tool in the complete redesign process is successfully demonstrated for the redesign of rotor 37 with an iterative optimization algorithm. The developed methodology is thus readily applicable to industrial blade models and offers an answer to the current lack of tools

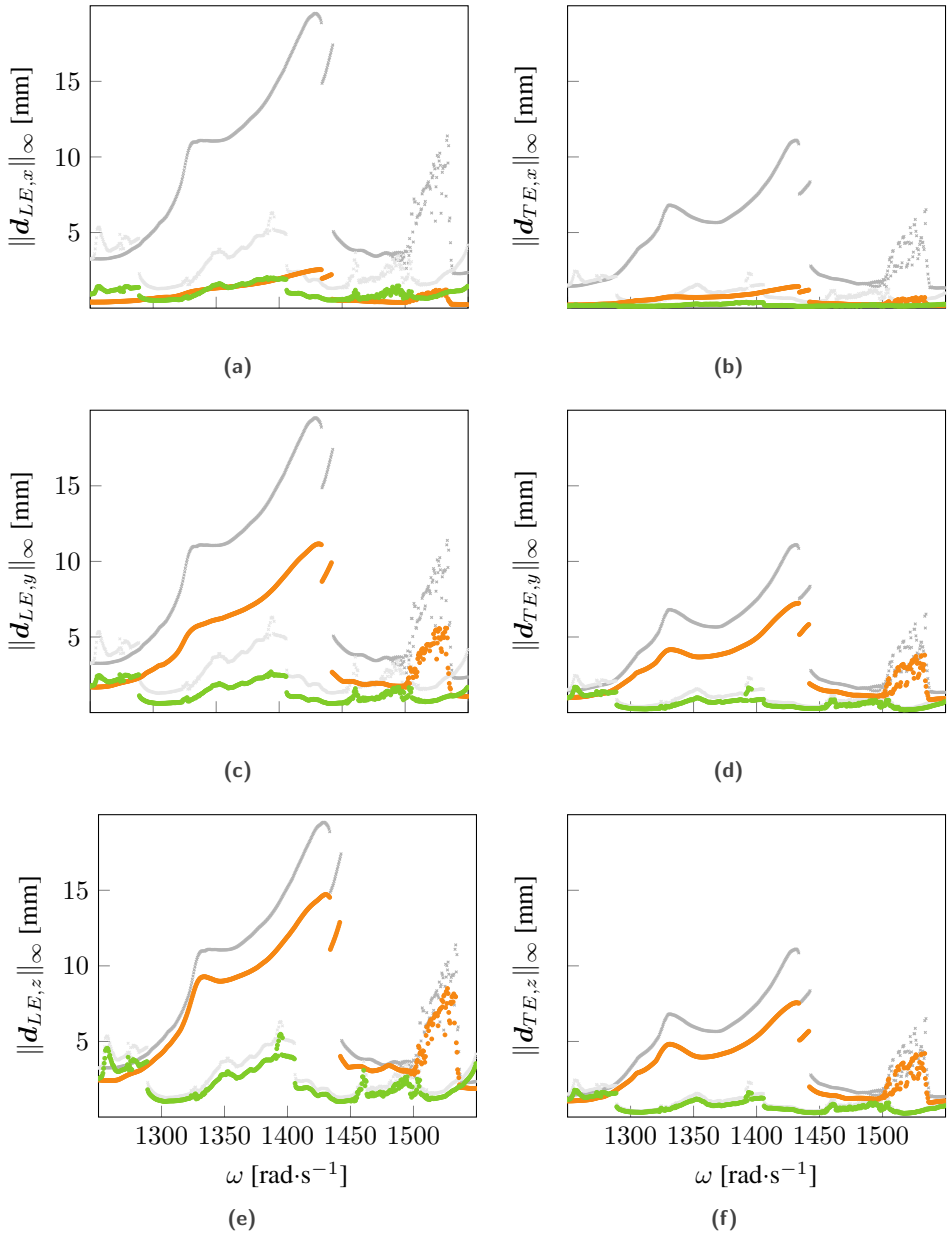

Figure 24. NFRC of Cartesian displacements for initial (——) and optimized (——) blades. NFRC of global displacement for initial (——) and optimized (——) blades.

dedicated to the design of blade robust to contact interactions.

The fidelity of the parameterized model could be improved further, *e.g.* by modifying the profile parameterization. Future works may involve the extensive use of the developed tool for the redesign of different blades accounting for robustness to contact interactions. Other performance criteria could be considered, as well as modification of the optimization algorithm to account for special characteristics of contact simulations, such as the presence of discontinuous quantities. Because the modularity of the tool has the potential to exhibit relationships between design variables and contact robustness, it is a powerful tool for the definition of original nonlinear dynamics design

criteria.

Appendix

5.1 Changes of basis equations

The changes of basis are described for some section $i \in \{1, ..., n_{\text{sec}}\}$. All angles are assumed to be in radians in the equations.

5.1.1 Transformation between $m_{\mathcal{B}_b}$ and $m_{\mathcal{B}_{s^i}}$

The relative placement of $\mathcal{B}_b$ and $\mathcal{B}_{s^i}$ bases depends of the type of section, as illustrated in Fig. 3. Changes of basis equations are detailed below for each type of section with cylindrical coordinates. The coordinates $\boldsymbol{k}^i|_{\mathcal{B}'_b}$ of a surface point $\boldsymbol{k}^i$ are required as equation parameters.

Conical section The point $\boldsymbol{k}^i$ is assumed to be different from the point $\boldsymbol{o}_{s^i}$ at the origin of the cone supporting the wrapped surface. For some section point $\boldsymbol{m}$, the change of basis equations are:

$$\begin{cases} m_{r,s^i} &= m_{r,b} \\ m_{\theta,s^i} &= \text{sgn}(\gamma^i) m_{\theta,b} \\ m_{z,s^i} &= \text{sgn}(\gamma^i)(m_{z,b} - o_{s^i z,b}) \end{cases} \iff \begin{cases} m_{r,b} &= m_{r,s^i} \\ m_{\theta,b} &= \text{sgn}(\gamma^i) m_{\theta,s^i} \\ m_{z,b} &= \text{sgn}(\gamma^i) m_{z,s^i} + o_{s^i z,b}, \end{cases} \tag{16}$$

where the coordinate $o_{s^i z,b}$ of the cone origin is given by: :

$$o_{s^i z,b} = \frac{-k^i_{r,b}}{\tan(\gamma^i)} + k^i_{z,b}, \quad \forall \gamma^i \neq 0. \tag{17}$$

Proof. Eq. (17) is first demonstrated. Generatrices of the wrapped surface are depicted in Fig. 25 in the half-plane$\{\boldsymbol{m} \in \mathbb{R}^3 : m_{y,b} = 0, m_{r,b} > 0\}$ for positive and negative conical sections. According to Fig. 25, the following equation holds:

$$l = |k^i_{z,b} - o_{s^i z,b}| = \frac{k^i_{r,b}}{\tan(|\gamma^i|)}.$$

For a positive conical section, $\gamma^i > 0$ and $k^i_{z,b} - o_{s^i z,b} > 0$, then from the previous equation, Eq. (17) is valid for

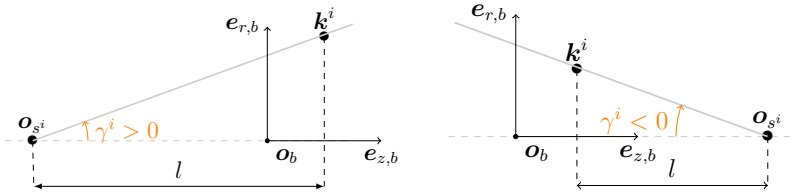

(a) positive conical section **(b)** negative conical section

Figure 25. Generatrices of conical wrapped surfaces in the half-plane $(\boldsymbol{o}_b, \boldsymbol{e}_{z,b}, \boldsymbol{e}^+_{r,b})$.

$\gamma^i > 0$. For a negative conical section, $\gamma^i < 0$ and $k^i_{z,b} - o_{s^i z,b} < 0$, then Eq. (17) is valid for $\gamma^i < 0$.

For a positive conical section ($\gamma^i > 0$), $\mathcal{B}_{s^i}$ is a translation of $\mathcal{B}_b$ along the $\boldsymbol{e}_{z,b}$ axis, and may thus be described by the following equations:

$$\begin{cases} m_{r,s^i} &= m_{r,b} \\ m_{\theta,s^i} &= m_{\theta,b} \\ m_{z,s^i} &= m_{z,b} - o_{s^i z,b} \end{cases} \quad \text{for } \gamma^i > 0. \tag{18}$$

For a negative conical section ($\gamma^i < 0$), $\mathcal{B}_{s^i}$ is a translation of $\mathcal{B}_b$ along the $\boldsymbol{e}_{z,b}$ axis followed by a rotation of π radians around the $\boldsymbol{e}_{x,s^i}$ axis, then:

$$\begin{cases} m_{r,s^i} &= m_{r_b} \\ m_{\theta,s^i} &= -m_{\theta,b} \\ m_{z,s^i} &= -m_{z,b} + o_{s^i z,b} \end{cases} \quad \text{for } \gamma^i < 0. \tag{19}$$

Eq. (16) is obtained by the aggregation of Eq. (18) and (19). □

Cylindrical section For some section point $\boldsymbol{m}$, the change of basis equations are:

$$\begin{cases} m_{r,s^i} &= m_{r,b} \\ m_{\theta,s^i} &= m_{\theta,b} \\ m_{z,s^i} &= m_{z,b} - k^i_{z,b} \end{cases} \iff \begin{cases} m_{r,b} &= m_{r,s^i} \\ m_{\theta,b} &= m_{\theta,s^i} \\ m_{z,b} &= m_{z,s^i} + k^i_{z,s^i}. \end{cases} \tag{20}$$

Proof. For a cylindrical section i, $\mathcal{B}_{s^i}$ is a translation of $\mathcal{B}_b$ along the $\boldsymbol{e}_{z,b}$ axis. The origin $\boldsymbol{o}_{s^i}$ of $\mathcal{B}_{s^i}$ is arbitrarily chosen so that $k^i_{z,s^i} = 0$. Hence equations (20) derive directly. □

5.1.2 Transformation between $m_{\mathcal{B}_{s^i}}$ and $m_{\mathcal{P}_{d^i}}$

The transformation describing the unwrapping of the surface from $\mathcal{B}_{s^i}$ to $\mathcal{P}_{d^i}$ and the relative position of these bases depends on the section type, see Fig. 4. This transformation is only valid for points belonging to the surface, which requires to introduce specific definition domains for each section type. The point $\boldsymbol{m}$ is assumed to belong to the surface in this section. The required equation parameters are the conicity γ^i for conical sections and the section radius r^i for cylindrical sections.

Conical section Let $\alpha = |\gamma^i|$ be the half-aperture of the conical wrapped surface of section i. The wrapped surface in $\mathcal{B}'_{s^i}$ depicted in Fig. 26 is described by the following set of points:

$$D_{\mathcal{B}'_{s^i}} = \{\boldsymbol{m}|_{\mathcal{B}'_{s^i}} : m_{z,s^i} \geq 0, m_{\theta,s^i} \in [-\pi, \pi[, m_{r,s^i} = m_{z,s^i} \tan\alpha\}.$$

The cone is unwrapped in the $(\boldsymbol{o}_{s^i}, \boldsymbol{e}_{x,s^i}, \boldsymbol{e}_{y,s^i})$ plane ; the unwrapped surface in $\mathcal{P}'_{d^i}$ is described by the following set of points:

$$D_{\mathcal{P}'_{d^i}} = \{\boldsymbol{m}|_{\mathcal{P}'_{d^i}} : m_{r,d^i} \geq 0, m_{\theta,d^i} \in [-\pi\sin\alpha, \pi\sin\alpha]\}.$$

Let $\boldsymbol{m}|_{\mathcal{B}'_{s^i}} \in D_{\mathcal{B}'_{s^i}}$ a point of the wrapped surface and $\boldsymbol{m}|_{\mathcal{P}'_{d^i}} \in D_{\mathcal{P}'_{d^i}}$ its image on the unwrapped surface. The transformation $f : D_{\mathcal{B}'_{s^i}} \to D_{\mathcal{P}'_{d^i}}$ is defined by:

$$\begin{cases} m_{r,d^i} &= \frac{m_{r,s^i}}{\sin(\alpha)} \\ m_{\theta,d^i} &= -m_{\theta,s^i}\sin(\alpha), \end{cases} \tag{21}$$

and the inverse transform $f^{-1} : D_{\mathcal{P}'_{d^i}} \to D_{\mathcal{B}'_{s^i}}$ is defined by:

$$\begin{cases} m_{r,s^i} &= m_{r,d^i}\sin(\alpha) \\ m_{\theta,s^i} &= -\frac{m_{\theta,d^i}}{\sin(\alpha)} \\ m_{z,s^i} &= m_{r,d^i}\cos(\alpha). \end{cases} \tag{22}$$

Proof. The distances from point $\boldsymbol{m}$ to the origin are unchanged by the unwrapping operation. Consequently:

$$\frac{m_{r,s^i}}{\sin(\alpha)} = l_1 = m_{r,d^i}. \tag{23}$$

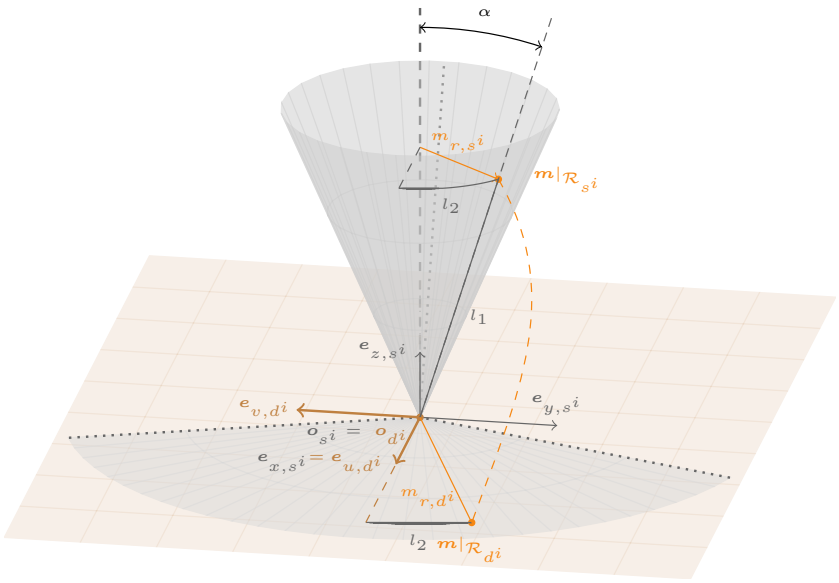

Figure 26. Wrapped conical surface in $\mathcal{B}'_{s^i}$ and unwrapped surface in $\mathcal{P}'_{d^i}$. Point $\boldsymbol{m}|_{\mathcal{B}'_{s^i}}$ on the wrapped surface and its image $\boldsymbol{m}|_{\mathcal{P}'_{d^i}}$ on the unwrapped surface.

Besides:

$$m_{z,s^i} = l_1 \cos(\alpha). \tag{24}$$

The arc lengths along the $\boldsymbol{e}_{\theta,s^i}$ direction on the wrapped surface are the same as the arc lengths along $-\boldsymbol{e}_{\theta,d^i}$ on the unwrapped surface. It follows that:

$$\begin{aligned} &-m_{r,s^i} m_{\theta,s^i} = m_{r,d^i} m_{\theta,d^i} \\ \iff \quad & m_{\theta,s^i} = -\frac{m_{\theta,d^i}}{\sin(\alpha)} \qquad \text{from (23)}. \end{aligned} \tag{25}$$

Eq. (22) is derived from Eq. (23), (24) and (25). Hence, Eq. (21) follows. □

Cylindrical section The wrapped surface of section i, depicted in Fig. 27, is described by the following set of points:

$$D_{\mathcal{B}'_{s^i}} = \{\boldsymbol{m}|_{\mathcal{B}'_{s^i}} : m_{r,s^i} = r^i, m_{\theta,s^i} \in [-\pi, \pi[, m_{z,s^i} \in \mathbb{R}\}.$$

The origin of $\mathcal{P}_{d^i}$ is defined by $\boldsymbol{o}_{d^i}|_{\mathcal{B}_{s^i}} = (r^i, 0, 0)$. The cylinder is unwrapped in the $(\boldsymbol{o}_{d^i}|_{\mathcal{B}_{s^i}}, \boldsymbol{e}_{y,s^i}, \boldsymbol{e}_{z,s^i})$ plane. The unwrapped surface is described by the following set of points:

$$D_{\mathcal{P}_{d^i}} = \{\boldsymbol{m}|_{\mathcal{P}_{d^i}} : m_{u,d^i} \in \mathbb{R}, m_{v,d^i} \in [-r^i\pi, r^i\pi[\}.$$

Let $\boldsymbol{m}|_{\mathcal{B}'_{s^i}} \in D_{\mathcal{B}'_{s^i}}$ a point of the wrapped surface and $\boldsymbol{m}|_{\mathcal{P}'_{d^i}} \in D_{\mathcal{P}'_{d^i}}$ the corresponding point on the unwrapped surface. The transformation $f : D_{\mathcal{B}'_{s^i}} \to D_{\mathcal{P}'_{d^i}}$ is defined by:

$$\begin{cases} m_{u,d^i} &= m_{z,s^i} \\ m_{v,d^i} &= -m_{r,s^i} m_{\theta,s^i}, \end{cases} \tag{26}$$

and the inverse transform $f^{-1} : D_{\mathcal{P}'_{d^i}} \to D_{\mathcal{B}'_{s^i}}$ is defined by:

$$\begin{cases} m_{r,s^i} &= r^i \\ m_{\theta,s^i} &= -\frac{m_{v,d^i}}{r^i} \\ m_{z,s^i} &= m_{u,d^i}. \end{cases} \tag{27}$$

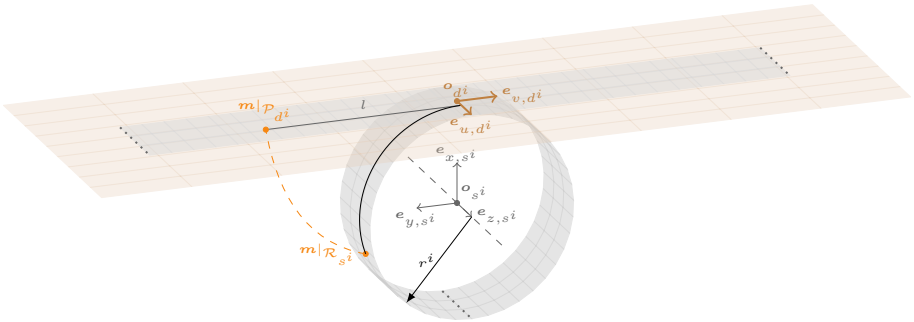

Figure 27. Wrapped cylindrical surface in $\mathcal{B}'_{s^i}$ and unwrapped surface in $\mathcal{P}_{d^i}$. Point $\boldsymbol{m}|_{\mathcal{B}'_{s^i}}$ on the wrapped surface and its image $\boldsymbol{m}|_{\mathcal{P}_{d^i}}$ on the unwrapped surface.

Proof. Assume that the coordinates $\boldsymbol{m}|_{\mathcal{B}'_{s^i}}$ are known. As shown in Fig. 27, the vectors $\boldsymbol{e}_{z,s^i}$ and $\boldsymbol{e}_{u,d^i}$ are identical, thus $m_{u,d^i} = m_{z,s^i}$. The coordinate m_{v,d^i} in absolute value is equal to the arc length on the cylinder, hence $m_{v,d^i} = l = -m_{r,s^i} m_{\theta,s^i}$. Hence Eq. (26) follows.

Assume now that the coordinates $\boldsymbol{m}|_{\mathcal{P}_{d^i}}$ are known. As $\boldsymbol{m}$ belongs to the wrapped surface, $m_{r,s^i} = r^i$. Eq. (27) derives from this and from Eq. (26). □

5.1.3 Transformation between $m_{\mathcal{P}_{d^i}}$ and $m_{\mathcal{P}_p}$

Let $\boldsymbol{m}$ be some section point. The transformation between the coordinates $\boldsymbol{m}|_{\mathcal{P}_p}$ and the coordinates $\boldsymbol{m}|_{\mathcal{P}_{d^i}}$ results from a rotation and a translation preserving the profile shape, see Fig. 28. The required equation parameters are the coordinates $\boldsymbol{n}^i|_{\mathcal{P}_p}$ and $\boldsymbol{n}^i|_{\mathcal{P}_{d^i}}$ of a section point $\boldsymbol{n}^i$ in both bases and the angle $(\widehat{\boldsymbol{e}_{u,d^i}, \boldsymbol{w}^i})$, where $\boldsymbol{w}^i$ is the chord vector defined in Eq. (4). Homogeneous coordinates denoted ${}^+\boldsymbol{m}|_{\mathcal{P}_\bullet} = (m_{u,\bullet}, m_{v,\bullet}, 1)$ are used in the following to facilitate the expression of the transformation. Elementary linear transformations are introduced prior to the complete transformation is stated.

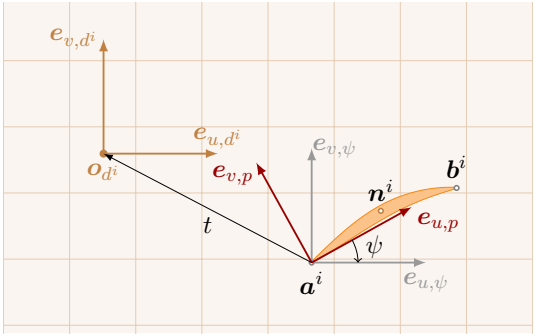

Figure 28. Two-dimensional Cartesian bases $\mathcal{P}_{d^i}$ and $\mathcal{P}_p$ and profile in $\mathcal{P}_p$ with arbitrary section point $\boldsymbol{n}^i$.

Elementary linear transformations Let $\mathcal{P}_1 = (\boldsymbol{o}_1, \boldsymbol{e}_{u,1}, \boldsymbol{e}_{v,1})$ and $\mathcal{P}_2 = (\boldsymbol{o}_2, \boldsymbol{e}_{u,2}, \boldsymbol{e}_{v,2})$ be two arbitrary two-dimensional Cartesian bases. Assume that $\mathcal{P}_2$ is the translation of $\mathcal{P}_1$ by a vector $\boldsymbol{t} = \boldsymbol{o}_2|_{\mathcal{P}_1}$. The homogeneous coordinates of $\boldsymbol{m}$ in both bases are linked by the translation matrix $\mathbf{T}_2^1$, denoted $\mathbf{T}(\boldsymbol{t})$:

$$ {}^+\boldsymbol{m}|_{\mathcal{P}_2} = \mathbf{T}_2^1 {}^+\boldsymbol{m}|_{\mathcal{P}_1}, \quad \text{with} \quad \mathbf{T}_2^1 = \mathbf{T}(\boldsymbol{t}) = \begin{bmatrix} 1 & 0 & -t_{u,1} \\ 0 & 1 & -t_{v,1} \\ 0 & 0 & 1 \end{bmatrix}. $$

The inverse transform is given by the relation ${}^+\boldsymbol{m}|_{\mathcal{P}_1} = \mathbf{T}(-\boldsymbol{t}) {}^+\boldsymbol{m}|_{\mathcal{P}_2}$.

Assume now that $\mathcal{P}_2$ is the rotation of $\mathcal{P}_1$ with respect to $\boldsymbol{o}_b$ from the angle $\psi = (\widehat{\boldsymbol{e}_{u,1}, \boldsymbol{e}_{u,2}})$. In this case, the homogeneous coordinates of $\boldsymbol{m}$ in both bases are linked by the rotation matrix $\mathbf{R}_2^1$, denoted $\mathbf{R}(\psi)$:

$$ {}^{+}\boldsymbol{m}|_{\mathcal{P}_2} = \mathbf{R}_2^1 {}^{+}\boldsymbol{m}|_{\mathcal{P}_1}, \quad \text{with} \quad \mathbf{R}_2^1 = \mathbf{R}(\psi) = \begin{bmatrix} \cos(\psi) & \sin(\psi) & 0 \\ -\sin(\psi) & \cos(\psi) & 0 \\ 0 & 0 & 1 \end{bmatrix}. $$

The inverse transform is given by the relation ${}^{+}\boldsymbol{m}|_{\mathcal{P}_1} = \mathbf{R}(-\psi) {}^{+}\boldsymbol{m}|_{\mathcal{P}_2}$.

Compound transformation The transformation from the coordinates ${}^{+}\boldsymbol{m}|_{\mathcal{P}_p}$ to the coordinates ${}^{+}\boldsymbol{m}|_{\mathcal{P}_{d^i}}$ is given by:

$$ {}^{+}\boldsymbol{m}|_{\mathcal{P}_{d^i}} = \mathbf{T}(\boldsymbol{t})\mathbf{R}(\psi) {}^{+}\boldsymbol{m}|_{\mathcal{P}_p}, \tag{28} $$

where $\psi = (\widehat{\boldsymbol{w}^i, \boldsymbol{e}_{u,d^i}})$ and $\boldsymbol{t}$ is deduced from ${}^{+}\boldsymbol{t} = \mathbf{R}(\psi) {}^{+}\boldsymbol{n}^i|_{\mathcal{P}_p} - {}^{+}\boldsymbol{n}^i|_{\mathcal{P}_{d^i}}$. The inverse transformation from ${}^{+}\boldsymbol{m}|_{\mathcal{P}_{d^i}}$ to ${}^{+}\boldsymbol{m}|_{\mathcal{P}_p}$ is thus given by:

$$ {}^{+}\boldsymbol{m}|_{\mathcal{P}_p} = \mathbf{R}(-\psi)\mathbf{T}(-\boldsymbol{t}) {}^{+}\boldsymbol{m}|_{\mathcal{P}_{d^i}}. \tag{29} $$

Proof. Bases $\mathcal{P}_p$ and $\mathcal{P}_{d^i}$ are shown in Fig. 28 along with one profile. An intermediate basis $\mathcal{P}_\psi$ is introduced as the rotation of $\mathcal{P}_p$ of the angle $\psi = -(\widehat{\boldsymbol{e}_{u,d^i}, \boldsymbol{w}^i})$. The transform from the coordinates ${}^{+}\boldsymbol{m}|_{\mathcal{P}_p}$ to the coordinates ${}^{+}\boldsymbol{m}|_{\mathcal{P}_\psi}$ may thus be written as:

$$ {}^{+}\boldsymbol{m}|_{\mathcal{P}_\psi} = \mathbf{R}(\psi) {}^{+}\boldsymbol{m}|_{\mathcal{P}_p}. \tag{30} $$

The basis $\mathcal{P}_{d^i}$ is a translation of $\mathcal{P}_\psi$ by a vector $\boldsymbol{t} = \boldsymbol{o}_d|_{\mathcal{P}_\psi}$ depicted in Fig 28. The transformation from ${}^{+}\boldsymbol{m}|_{\mathcal{P}_\psi}$ to ${}^{+}\boldsymbol{m}|_{\mathcal{P}_{d^i}}$ may thus be written as:

$$ {}^{+}\boldsymbol{m}|_{\mathcal{P}_{d^i}} = \mathbf{T}(\boldsymbol{t}) {}^{+}\boldsymbol{m}|_{\mathcal{P}_\psi}. \tag{31} $$

By definition, $\boldsymbol{t} = \boldsymbol{o}_d|_{\mathcal{P}_\psi} = \boldsymbol{o}_d|_{\mathcal{P}_\psi} - \boldsymbol{o}_d|_{\mathcal{P}_{d^i}}$. All the profile points undergo the same translation, hence $\boldsymbol{t} = (t_u, t_v)$ may be computed from ${}^{+}\boldsymbol{n}^i|_{\mathcal{P}_p}$ and ${}^{+}\boldsymbol{n}^i|_{\mathcal{P}_{d^i}}$:

$$ \begin{aligned} (t_u, t_v, 0) &= {}^{+}\boldsymbol{n}^i|_{\mathcal{P}_\psi} - {}^{+}\boldsymbol{n}^i|_{\mathcal{P}_{d^i}} \\ &= \mathbf{R}(\psi) {}^{+}\boldsymbol{n}^i|_{\mathcal{P}_p} - {}^{+}\boldsymbol{n}^i|_{\mathcal{P}_{d^i}} \text{ from (31).} \end{aligned} \tag{32} $$

Eq. (28) follows directly from Eq. (30) and (31). Hence Eq. (29) is straightforward. □

5.1.4 Determination of equation parameters in *GEN* module

The equation parameters required for the change of bases in `GEN` module must be computed from the stacking parameters provided in input of the module. Equations parameters depend on the type of section.

Conical section

Proof of Eq.(6), (7) *and* (8). The coordinates $\boldsymbol{q}^i|_{\mathcal{P}_{d^i}}$ are first given with respect to the coordinates $\boldsymbol{q}^i|_{\mathcal{B}_b}$. For q^i_{u,d^i} the following equations hold:

$$ \begin{aligned} q^i_{u,d^i} &= q^i_{r,d^i} \cos(q^i_{\theta,d^i}) \\ &= \frac{q^i_{r,s^i}}{\sin|\gamma^i|} \cos(-q^i_{\theta,s^i} \sin(|\gamma^i|)) && \text{from (21)} \\ &= \frac{q^i_{r,b}}{\sin|\gamma^i|} \cos(-\operatorname{sgn}(\gamma^i) q^i_{\theta,b} \sin(|\gamma^i|)) && \text{from (16).} \end{aligned} $$

A similar equation may be derived for q^i_{v,d^i}:

$$q^i_{v,d^i} = \frac{q^i_{r,b}}{\sin(|\gamma^i|)} \sin(-\operatorname{sgn}(\gamma^i) q^i_{\theta,b} \sin(|\gamma^i|)).$$

From the definitions of r^i in Eq. (1) and $\Delta\theta^i$ in Eq. (2), Eq. (6) and (7) derive directly from the expressions of q^i_{u,d^i} and q^i_{v,d^i}. The chord angle $(\widehat{\boldsymbol{e}_{u,d^i}, \boldsymbol{w}^i})$ may be divided into two angles such as:

$$(\widehat{\boldsymbol{e}_{u,d^i}, \boldsymbol{w}^i}) = (\widehat{\boldsymbol{e}_{u,d^i}, \boldsymbol{v}^i}) + (\widehat{\boldsymbol{v}^i, \boldsymbol{w}^i}), \tag{33}$$

with $\boldsymbol{v}^i = \boldsymbol{q}^i|_{\mathcal{P}_{d^i}} / \|\boldsymbol{q}^i|_{\mathcal{P}_{d^i}}\|$. On the one hand, the first angle satisfies:

$$\begin{aligned} (\widehat{\boldsymbol{e}_{u,d^i}, \boldsymbol{v}^i}) &= q^i_{\theta,d^i} \\ &= -\operatorname{sgn}(\gamma^i) q^i_{\theta,b} \sin(|\gamma^i|) && \text{from (21) and (16)} \\ &= -\operatorname{sgn}(\gamma^i) \Delta\theta^i \sin(|\gamma^i|) && \text{by definition of } \Delta\theta^i \text{ (2).} \end{aligned} \tag{34}$$

The angle $(\widehat{\boldsymbol{v}^i, \boldsymbol{w}^i})$ is directly derived from the stagger angle λ^i defined in Eq. (5):

$$(\widehat{\boldsymbol{v}^i, \boldsymbol{w}^i}) = \begin{cases} \lambda^i & \text{for a positive conical section,} \\ \lambda^i - \pi & \text{for a negative conical section.} \end{cases} \tag{35}$$

Thus Eq. (8) follows from Eq. (33), (34) and (35). □

Cylindrical section

Proof of Eq. (9). The coordinate q^i_{u,d^i} is given by:

$$q^i_{u,d^i} \underbrace{=}_{\text{from (26)}} q^i_{z,s^i} \underbrace{=}_{\text{from (20)}} q^i_{z,b} - k^i_{z,b}. \tag{36}$$

In the `GEN` module, the point $\boldsymbol{k}^i$ is chosen such as $\boldsymbol{k}^i|_{\mathcal{B}'_b} = (r^i, 0, \Delta z^i)$. Thus from Eq. (36), $q^i_{u,d^i} = \Delta z^i - \Delta z^i = 0$. The coordinate q^i_{v,d^i} is given by:

$$q^i_{u,v^i} \underbrace{=}_{\text{from (26)}} -q^i_{r,s^i} q^i_{\theta,s^i} \underbrace{=}_{\text{from (20)}} -q^i_{r,b} q^i_{\theta,b} \underbrace{=}_{\text{from (1) and (2)}} -r^i \Delta\theta^i. \tag{37}$$

Finally, by definition of the stagger angle at Eq. (5), the chord angle satisfies $(\widehat{\boldsymbol{e}_{u,d^i}, \boldsymbol{w}^i}) = \lambda^i$. Hence and from Eq. (36) and (37), Eq. (9) follows. □

5.2 Parameterized model of rotor 37

The blades parameters of rotor 37 obtained with the `PAR` module and $n_{\text{sec}} = 3$ are shown in Table 6.

5.3 Simulation parameters

Contact simulations are conducted in this work according to a published numerical strategy based on time integration [42]. Simulations parameters are shown in Table 7 for rotor 37 models and in Table 8 for rotor 67 models.

Table 6. Blade parameters of rotor 37 identified from PAR module with $n_{\text{sec}} = 3$.

parameter	section 1	section 2	section 3
r^i	182.235	215.563	248.570
$\Delta\theta^i$	0.000	−0.070	−0.189
Δz^i	0.000	0.647	1.079
γ^i	12.600	−1.320	−15.240
λ^i	38.725	50.564	60.518
$s^i_{u.p}$	31.752	33.544	40.040
$s^i_{v.p}$	6.754	3.884	2.505
$p^i_{v.p}$	34.981	37.749	45.928
c^i	57.003	56.285	56.336
t^i	4.555	3.076	1.774
r^i_{LE+}	0.875	0.606	0.292
r^i_{LE-}	0.352	0.287	0.251
r^i_{TE}	0.225	0.226	0.061
ϕ^i_{LE}	4.622	0.209	0.603
ψ^i_{LE+}	12.474	8.138	4.094
ψ^i_{LE-}	1.974	0.010	0.000
ϕ^i_{TE}	19.944	8.438	18.089
ψ^i_{TE+}	9.967	10.195	0.000
ψ^i_{TE-}	8.180	1.436	14.317

5.4 Validation of robustness and computational efficiency

5.4.1 Computational efficiency

The computation time of GEN and MSH modules from rotor 37 blade parameters are shown in Fig. 29a for $n_{\text{sec}} = \{2, 3, 5, 9, 17\}$. These parameters are obtained with the extraction procedure described in Sec. 2.3. The GEN module is responsible for the major part of the computation time. This part increases with n_{sec} because the CAD model generation is longer when the number of interpolated sections increases. However, the total computation time does not exceed 13.5 s for the 5-section parameterized model used in the iterative redesign process. This time is acceptable with respect to the simulation time of the dynamic clearance of about 30 sec. As the dynamic clearance is a relatively cheap performance criterion, the comparison will remain valid for future contact criteria.

The computation time of the PAR module applied to the input blade rotor 37 in shown in Fig. 29b with respect to n_{sec}. About 98% of the computation time are dedicated to the identification of profile parameters in Problem (13); around 5 min are required for each profile. As the PAR module is only used once at the beginning of the redesign process, its computation time is considered negligible with respect to the total time of the iterative process (about 3.5 hours).

5.4.2 Robustness

The robustness of the GEN module with respect to n_{sec} is demonstrated in Sec. 3 by generating CAD models up to $n_{\text{sec}} = 17$. The robustness of this module is here assessed with respect to the variation of stacking parameters along the blade height.

From the 5-section model of rotor 37, 4 blades are generated: the profile parameters of the mid-span section of rotor 37 are used for all sections, and the section radii of rotor 37 are preserved. For each blade, one of the remaining stacking parameters is varied linearly from the hub to the top of the blade. For illustration purposes,

Table 7. Parameters for the contact simulations with rotor 37 models.

time integration	time step [s]	5×10^{-8}
	blade revolutions	200
	angular speed range [rad·s^{-1}]	$[1250, 1550]$
contact scenario	number of lobes	2
	factor defining angular width of lobes	0.15
	lobe height [m]	6.25×10^{-4}
	clearance [m]	5×10^{-4}
	friction coefficient	0.15
reduced-order model	number of fixed interface modes	10
	number of boundary nodes	8
	modal damping coeff. (first-three free-vibration modes)	0.001
	modal damping coeff. (other free-vibration modes)	0.005

Table 8. Parameters for the contact simulations with rotor 67 models.

time integration	time step [s]	5×10^{-8}
	blade revolutions	200
	angular speed range [rad·s^{-1}]	$[900, 1780]$
contact scenario	number of lobes	2
	factor defining angular width of lobes	0.15
	lobe height [m]	5.25×10^{-4}
	clearance [m]	4×10^{-4}
	friction coefficient	0.15
reduced-order model	number of fixed interface modes	10
	number of boundary nodes	8
	modal damping coeff. (first-free free-vibration modes)	0.001
	modal damping coeff. (other free-vibration modes)	0.005

unrealistic extreme variations are considered. For blade (a) in Fig.30, γ^i is varied from $-\pi/2$ to $\pi/2$; beyond these values the CAD model is generated without errors but some surfaces are intersected. For blade (b), the quantity $\Delta\theta^i$ is varied from 0 to $\frac{2}{3}\pi$ and for blade (c), Δz^i is varied from 0 to 5 times the blade height. The variation of λ^i from 0 to $\pi/2$, a limit value for compressor blade, is illustrated with blade (d). All four blades were generated without errors or additional computation time, which attests of the robustness of the `GEN` module.

Acknowledgements

This research was undertaken thanks to funding from the discovery grant RGPIN-2020-04448 from the Natural Sciences and Engineering Research Council of Canada (second author), the Canada Research Chairs Program, Funder ID: 10.13039/ 501100001804(third author) and the Merit Scholarship for Foreign Students (PBEEE) from FRQNT (first author).

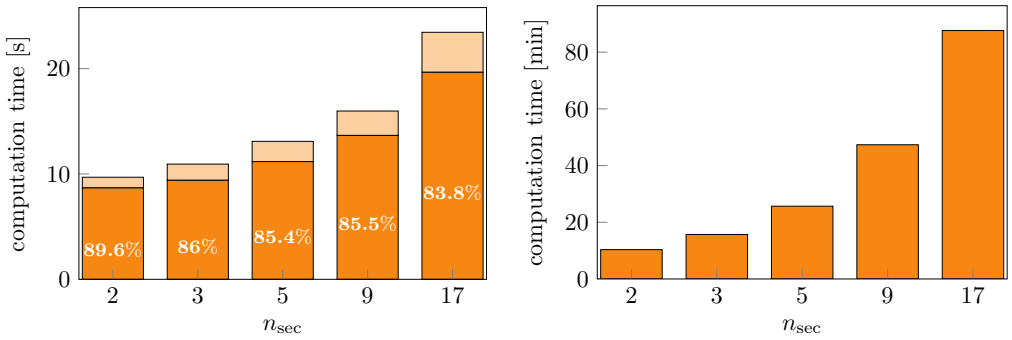

(a) `GEN` (■) and `MSH` (□) modules **(b)** `PAR` module

Figure 29. Computation time of `GEN`, `MSH` and `PAR` modules applied on rotor 37 for $n_{\text{sec}} \in \{2, 3, 5, 9, 17\}$.

(a) variation of γ^i **(b)** variation of $\Delta\theta^i$ **(c)** variation of Δz^i **(d)** variation of λ^i

Figure 30. Blades computed with extreme linear variations of stacking parameters along the blade height.

References

[1] Safran Helicopter Engines. *Final Report Summary - E-BREAK (Engine Breakthrough Components and Subsystems)*. Tech. rep. accessed 22 Nov. 2021. European Comission, 2017. URL: https://cordis.europa.eu/project/id/314366/reporting.

[2] C. J. Hulme, S. W. Fiebiger, and J. Szwedowicz. "Axial Compressor Blade Failure, Design Modification, and its Validation". In: *ASME Turbo Expo*. Turbo Expo: Power for Land, Sea, and Air. Montreal, Canada, 2015. DOI: 10.1115/GT2015-43312.

[3] A. Torkaman, G. Vogel, S. Fiebiger, D. Dietrich, and R. Washburn. "Gas Turbine Cycle Upgrade and Validation for Heavy Duty Industrial Machines". In: *Turbo Expo: Power for Land, Sea, and Air*. Vol. 3: Coal, Biomass and Alternative Fuels; Cycle Innovations; Electric Power; Industrial and Cogeneration Applications; Organic Rankine Cycle Power Systems. 2017. DOI: 10.1115/GT2017-64173.

[4] Y. Lu, B. Lad, and M. Vahdati. "Transonic Fan Blade Redesign Approach to Attenuate Nonsynchronous Vibration". In: Journal of Engineering for Gas Turbines and Power Vol. 143, No. 7 (2021). DOI: 10.1115/1.4050023.

[5] M. Krack, L. Salles, and F. Thouverez. "Vibration Prediction of Bladed Disks Coupled by Friction Joints". In: Archives of Computational Methods in Engineering Vol. 24, No. 3 (2017), 589–636. DOI: 10.1007/s11831-016-9183-2. OAI: hal.archives-ouvertes.fr/hal-01825517.

[6] H. Ma, F. Yin, Y. Guo, X. Tai, and B. Wen. "A review on dynamic characteristics of blade–casing rubbing". In: Nonlinear Dynamics Vol. 84, No. 2 (2016), 437–472. DOI: 10.1007/s11071-015-2535-x.

[7] N. Salvat, A. Batailly, and M. Legrand. "Two-dimensional modeling of unilateral contact-induced shaft precessional motions in bladed-disk/casing systems". In: International Journal of Non-Linear Mechanics Vol. 78 (2016), 90–104. DOI: 10.1016/j.ijnonlinmec.2015.10.001. URL: https://publications.polymtl.ca/10854/.

[8] Bondyra, Radoslaw, Dominiczak, Krzysztof, and Matuszak, Jacek. "Reverse engineering methodology as a way of steam turbine blades designing for Loviisa Nuclear Power". In: E3S Web Conf. Vol. 137 (2019), 01002. DOI: 10.1051/e3sconf/201913701002. URL: https://www.e3s-conferences.org/articles/e3sconf/abs/2019/63/e3sconf_rdpe2019_01002/e3sconf_rdpe2019_01002.html.

[9] Y.-K. Jung, K. Chang, S.-H. Park, V. T. Ho, H.-J. Shim, and M.-W. Kim. "Reverse Engineering and Database of Off-the-Shelf Propellers for Middle-Size Multirotors". In: Unmanned Systems Vol. 9, No. 4 (2021), 321–332. DOI: 10.1142/S2301385021500163.

[10] K. Cui, W. Wang, R. Jiang, and D. Zhao. "Model reconstruction in adaptive machining for near-net-shape rolling compressor blades". In: International Journal of Computer Integrated Manufacturing Vol. 31, No. 2 (2018), 138–151. DOI: 10.1080/0951192X.2017.1407454.

[11] L. Chen, B. Li, Z. Jiang, J. Ding, and F. Zhang. "Parameter extraction of featured section in turbine blade inspection". In: *2010 IEEE International Conference on Automation and Logistics*. 2010, pp. 501–505. DOI: 10.1109/ICAL.2010.5585336.

[12] F. Bauer, M. Schrapp, and J. Szijarto. "Accuracy analysis of a piece-to-piece reverse engineering workflow for a turbine foil based on multi-modal computed tomography and additive manufacturing". In: Precision Engineering Vol. 60 (2019), 63–75. DOI: 10.1016/j.precisioneng.2019.07.008.

[13] G. Persico, P. Rodriguez-Fernandez, and A. Romei. "High-Fidelity Shape Optimization of Non-Conventional Turbomachinery by Surrogate Evolutionary Strategies". In: Journal of Turbomachinery Vol. 141, No. 8 (2019). DOI: 10.1115/1.4043252.

[14] Y. Rong, J. Xu, and Y. Sun. "A surface reconstruction strategy based on deformable template for repairing damaged turbine blades". In: Proceedings of the Institution of Mechanical Engineers, Part G: Journal of Aerospace Engineering Vol. 228, No. 12 (2014), 2358–2370. DOI: 10.1177/0954410013517091.

[15] S. Slyadnev and V. Turlapov. "To the Development of Open Source Software for the Reconstruction of CAD Models". In: Programming and Computer Software Vol. 45, No. 4 (2019), 202–12. DOI: 10.1134/S036176881904008X.

[16] K. Mohaghegh, M. H. Sadeghi, A. Abdullah, and R. Boutorabi. "Improvement of reverse-engineered turbine blades using construction geometry". In: The International Journal of Advanced Manufacturing Technology Vol. 49, No. 5 (2010), 675–687. DOI: 10.1007/s00170-009-2409-9.

[17] R. Alexeev, V. Tishchenko, V. Gribin, and I. Gavrilov. "Turbine blade profile design method based on Bezier curves". In: Journal of Physics: Conference Series Vol. 891 (2017), 012254. DOI: 10.1088/1742-6596/891/1/012254. eprint: www.euroturbo.eu/paper/ETC2017-195.pdf.

[18] Y. Li, X. Huang, C. Gong, and K. Wang. "An engineering rules based parameterization approach for turbine blade reverse engineering". In: *Geometric Modeling and Processing, 2004. Proceedings.* 2004, pp. 311–318. DOI: 10.1109/GMAP.2004.1290052.

[19] Y. Zhou, Y. Song, T. Xing, Y. Wang, Q. Zhang, L. Shao, F. Du, and S. Ding. "Parametric modeling method for integrated design and manufacturing of radial compressor impeller". In: International Journal of Advanced Manufacturing Technology Vol. 112, No. 3-4 (2021), 1007–1021. DOI: 10.1007/s00170-020-06331-5.

[20] J. Lainé, E. Piollet, F. Nyssen, and A. Batailly. "Blackbox optimization for aircraft engine bladed components featuring contact interfaces". In: Journal of Engineering for Gas Turbines and Power Vol. 141, No. 6 (2019). DOI: 10.1115/1.4042808. OAI: hal.inria.fr/hal-02059582v1.

[21] A. Batailly, M. Legrand, A. Millecamps, S. Cochon, and F. Garcin. "Redesign of a high-pressure compressor blade accounting for nonlinear structural interactions". In: J Eng Gas Turbines Power Vol. 137, No. 2 (2015), 022502. DOI: 10.1115/1.4028263. OAI: hal.archives-ouvertes.fr/hal-01120158.

[22] R. Agromayor, N. Anand, J.-D. Müller, M. Pini, and L. O. Nord. "A Unified Geometry Parametrization Method for Turbomachinery Blades". In: Computer-Aided Design Vol. 133 (2021), 102987. DOI: 10.1016/j.cad.2020.102987.

[23] B. Wu, H. Zheng, Y. Zhang, M. Luo, and D. Zhang. "A Model Reconstruction Method of Blade Repair Based on Linear Combination". In: International Journal of Precision Engineering and Manufacturing Vol. 22, No. 3 (2021), 383–394. DOI: 10.1007/s12541-020-00449-y.

[24] E. Benini. "Three-Dimensional Multi-Objective Design Optimization of a Transonic Compressor Rotor". In: Journal of Propulsion and Power Vol. 20, No. 3 (2004), 559–565. DOI: 10.2514/1.2703.

[25] Q. Agrapart, F. Nyssen, D. Lavazec, P. Dufrénoy, and A. Batailly. "Multi-physics numerical simulation of an experimentally predicted rubbing event in aircraft engines". In: Journal of Sound and Vibration Vol. 460 (2019), 114869. DOI: 10.1016/j.jsv.2019.114869. OAI: hal.science/hal-02269517.

[26] A. Batailly, M. Legrand, and C. Pierre. "Full three-dimensional rotor/stator interaction simulations in aircraft engines with time-dependent angular speed". In: Journal of Engineering for Gas Turbines and Power Vol. 139, No. 3 (2017), 031202. DOI: 10.1115/1.4034503. OAI: hal.archives-ouvertes.fr/hal-03444757.

[27] E. P. Petrov. "Multiharmonic Analysis of Nonlinear Whole Engine Dynamics With Bladed Disc-Casing Rubbing Contacts". In: *ASME Turbo*. Vol. 7: Structures and Dynamics, Parts A and B. Turbo Expo: Power for Land, Sea, and Air. 2012, pp. 1181–1191. DOI: 10.1115/GT2012-68474.

[28] Y. Zhang and Z.-T. Chen. "Constraints and CFD simulation-based parametric reconstruction for 2D blade profile in reverse engineering". In: Proceedings of the Institution of Mechanical Engineers, Part G: Journal of Aerospace Engineering Vol. 230, No. 12 (2016), 2137–2146. DOI: 10.1177/0954410015621087.

[29] A. Batailly, Q. Agrapart, A. Millecamps, and J.-F. Brunel. "Experimental and numerical simulation of a rotor/stator interaction event localized on a single blade within an industrial high-pressure compressor". In: Journal of Sound and Vibration Vol. 375 (2016), 308–331. DOI: 10.1016/j.jsv.2016.03.016. OAI: hal.science/hal-01342401.

[30] L. Pacyna, A. Bertret, A. Derclaye, L. Papeleux, and J.-P. Ponthot. "Implementation of a Rig Test for Rotor/Stator Interaction of Low-Pressure Compressor Blades and Comparison of Experimental Results With Numerical Model". In: *ASME Turbo Expo*. Vol. 11: Structures and Dynamics: Structural Mechanics, Vibration, and Damping; Supercritical CO2. Turbo Expo: Power for Land, Sea, and Air. V011T30A006. 2020. DOI: 10.1115/GT2020-14266.

[31] Y. Colaïtis and A. Batailly. "Development of a harmonic balance method-based numerical strategy for blade-tip/casing interactions: application to NASA rotor 37". In: Journal of Engineering for Gas Turbines and Power (2021). DOI: 10.1115/1.4051967. OAI: hal.archives-ouvertes.fr/hal-03343050.

[32] E. Piollet. "Blade/casing rubbing interactions in aircraft engines: numerical benchmark and design guidelines based on NASA rotor 37". In: Journal of Sound and Vibration Vol. 460 (2019), 114878. DOI: 10.1016/j.jsv.2019.114878. OAI: hal.archives-ouvertes.fr/hal-02281666.

[33] M. de Cherisey, L. Salles, L. Renson, A. Vizzaccaro, and C. Wong. "Optimization of a Turbomachinery Blade With Regards to Tip-Rub Events". In: vol. Volume 8B: Structures and Dynamics — Probabilistic Methods; Rotordynamics; Structural Mechanics and Vibration. Turbo Expo: Power for Land, Sea, and Air. V08BT27A013. 2022. DOI: 10.1115/GT2022-82005. URL: https://doi.org/10.1115/GT2022-82005.

[34] L. Reid and R. D. Moore. *Design and overall performance of four highly loaded, high speed inlet stages for an advanced high-pressure-ratio core compressor*. Tech. rep. accessed 22 Nov. 2021. NASA, 1978. URL: https://ntrs.nasa.gov/citations/19780025165.

[35] D. C. Urasek, W. S. Cunnan, and W. Stevans. *Performance of two-stage fan with larger dampers on first-stage rotor*. Tech. rep. accessed 22 Nov. 2021. NASA, 1979. URL: https://ntrs.nasa.gov/citations/19790015796.

[36] C. Audet and J. J.E. Dennis. "Mesh Adaptive Direct Search Algorithms for Constrained Optimization". In: SIAM Journal on Optimization Vol. 17, No. 1 (2006), 188–217. DOI: 10.1137/040603371.

[37] E. Piollet and A. Batailly. A program to compute compressor blade geometries from multiple-circular-arc parameters with sweep and lean (v1.0)[source code]. 2019. URL: https://hal.archives-ouvertes.fr/hal-02127993.

[38] J. Lainé. "Optimisation d'aubes de turbomachines : minimisation de la réponse vibratoire à la suite de contacts avec le carter". MA thesis. École Polytechnique de Montréal, 2017. URL: https://publications.polymtl.ca/2897/.

[39] S. Le Digabel. "Algorithm 909: NOMAD: Nonlinear Optimization with the MADS algorithm". In: ACM Transactions on Mathematical Software Vol. 37, No. 4 (2011), 44:1–44:15. DOI: 10.1145/1916461.1916468.

[40] T. Korakianitis and P. Papagiannidis. "Surface-Curvature-Distribution Effects on Turbine-Cascade Performance". In: Journal of Turbomachinery Vol. 115, No. 2 (1993), 334–341. DOI: 10.1115/1.2929239.

[41] A. Batailly and A. Millecamps. "Minimising clearance consumption: a key factor for the design of blades robust to rotor/stator interactions?" In: *ASME Turbo Expo*. Turbo Expo: Power for Land, Sea, and Air. Séoul, South Korea, 2016. DOI: 10.1115/GT2016-56721.

[42] A. Batailly, M. Legrand, A. Millecamps, and F. Garcin. "Numerical-experimental comparison in the simulation of rotor/stator interaction through blade-tip/abradable coating contact". In: Journal of Engineering for Gas Turbines and Power Vol. 134, No. 8 (2012), 082504. DOI: 10.1115/1.4006446. OAI: hal.archives-ouvertes.fr/hal-00746632.

[43] R. R. Craig and M. C. C. Bampton. "Coupling of Substructures for Dynamic Analyses". In: AIAA Journal Vol. 6, No. 7 (1968), 1313–1319. DOI: 10.2514/3.4741. OAI: hal.archives-ouvertes.fr/hal-01537654.

[44] R. Seydel. Practical Bifurcation and Stability Analysis. Vol. 5. 2010. DOI: /10.1007/978-1-4419-1740-9.